7
Activated-Tungsten Inert Gas (A-TIG) Welding

This chapter focuses on experiments that will aid in achieving a complete depth of penetration of up to 8 mm using different fluxes and their combination by utilizing the phenomenon of reversal of Marangoni convection in the molten weld pool. The welding technique used in this chapter is tungsten inert gas welding (TIG) as it provides more accurate control over the welding arc, hence activated-tungsten inert gas (A-TIG) welding.

7.1 BEAD-ON-PLATE EXPERIMENTS

The plates of dimension 130 mm × 50 mm × 8 mm were conventionally machined and prepared out of P91 and Incoloy 800HT base metal plates. One plate of P91 was used to obtain bead-on-plate welds using SiO2 flux with varying welding current, and the second plate of P91 was used to obtain bead-on-plate welds using TiO_2 flux with varying welding current. The flux was mixed with acetone to obtain a paste-like consistency and was applied with a paintbrush. In the same fashion, bead-on-plate welds were obtained for Incoloy 800HT plates. The welding current in the consecutive single autogenous welding passes was varied as 180 A, 200 A, 220 A, 240 A, and 260 A. Thoriated tungsten electrode with 2.9 mm diameter and 60˚ tip angle was used. A constant arc length of 3 mm and travel speed of 80 mm/min were maintained for each pass. The schematic in Figure 7.1 depicts the sequence and position of the bead on plate welds. The metallographic specimens were extracted on a band saw and using convention machining. The metallographic samples were mirror polished, P91 was etched using Vilella's reagent, and Incoloy 800HT was electrolytically etched in 10% oxalic acid solution. Then, macrostructure observation was observed on a stereo microscope, and microstructure was observed on a Leica optical microscope.

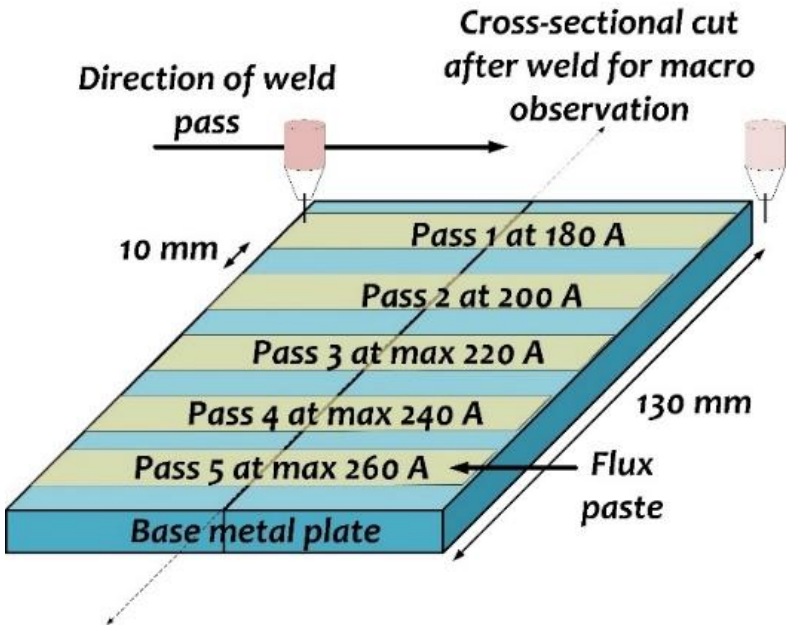


Figure 7.1 : Schematics of bead on plate weld sequence employing A-TIG welding

7.1.1 Macroscopic Observations

After the bead-on-plate weld was completed, the plates the cut into a cross-section to observe the macrostructure. Figure 7.2 shows the top face of the weld beads obtained; as observed for all the bead-on-plate welds made, the weld bead width increases with an increase in current. Also, clean and linear weld beads are obtained with no slag formation. Figure 7.2(a-b) depicts the weld beads obtained for SiO_2 and TiO_2 flux, respectively. While Figure 7.2(c-d) depicts the weld bead obtained for SiO_2 and TiO_2 flux, respectively. Figure 7.3(a-e) shows the macrostructure observed for bead on-plate weld on Incoloy 800HT plate using the SiO_2 flux, and it can be observed that the DOP kept increasing with current, and maximum penetration was observed at 260 A. Also, the weld bead width was observed to increase with the current. Figure 7.3(f-j) shows the macrostructure observed for a bead on plate weld on an Incoloy 800HT plate using the TiO_2 flux; here, the maximum DOP was observed to be increasing with an increase in current, stabilizing, and then it decreased. However, the width of the weld bead increased with an increase in current. Figure 7.4(a-e) shows the macrostructure observed for bead-on-plate welds on the P91 plate using the SiO_2 flux. Figure 7.4(c) was observed with maximum penetration, and overall, the depth of penetration increased initially and then decreased with an increase in current for SiO_2 flux on the P91 plate (Vidyarthy et al., 2017). Weld bead width showed an inverse proportion relation with the depth of penetration as it decreased with an increase in penetration. However, with increasing welding current, penetration decreased again, and weld bead width was observed to increase significantly. Figure 7.4(f-j) shows the macrostructure observed for a bead-on-plate weld on the P91 plate using the TiO_2 flux. The DOP increased with an increase in current, and a complete DOP was observed at 260 A, as shown in Figure 7.4(j). However, a slight odd decrease in the DOP was observed at 220 A. Compared to the trend of weld bead width in the case of SiO_2 flux on the P91 plate, weld bead width increased with an increase in current. The SiO_2 flux on the P91 plate showed some increase in DOP, but no significant increase was observed with SiO_2 flux for either P91 or Incoloy 800HT. Also, its effects on weld bead width suggest that it reacted differently with P91 as varying results were obtained. TiO_2 flux showed completed penetration and signs of reversal of Marangoni convection in P91 at 260 A; however, it didn't perform well in the case of Incoloy 800HT and gave maximum penetration at 220 A. TiO_2 flux showed a consistent increase in weld bead width with an increase in current in both the cases. The measured weld bead width and depth of penetration data for observed macrostructures are presented in Table 7.1.

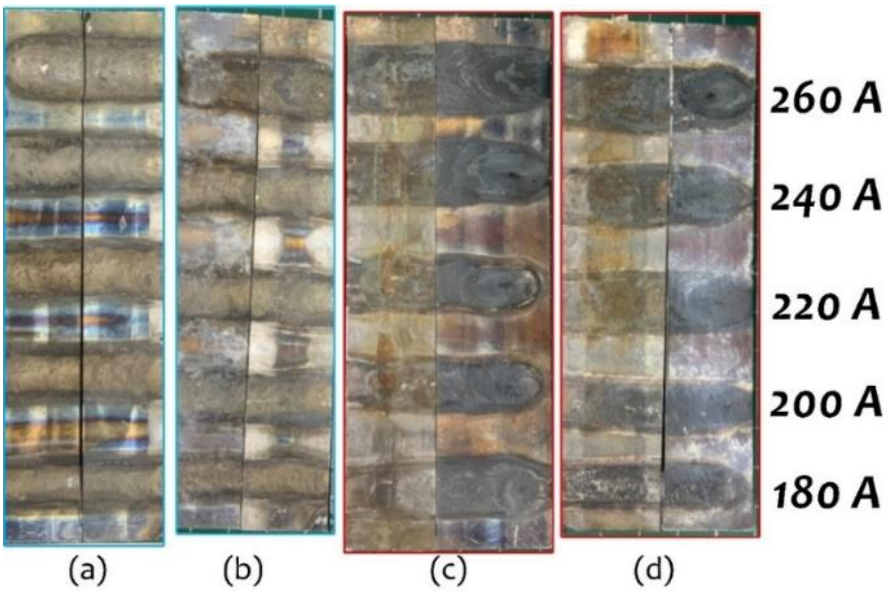


Figure 7.2 : Bead on plate welds: (a) with SiO_2 flux on Incoloy 8000HT plate (b) with TiO_2 flux on Incoloy 8000HT plate (c) with SiO_2 flux on P91 plate (d) with TiO_2 flux on P91 plate

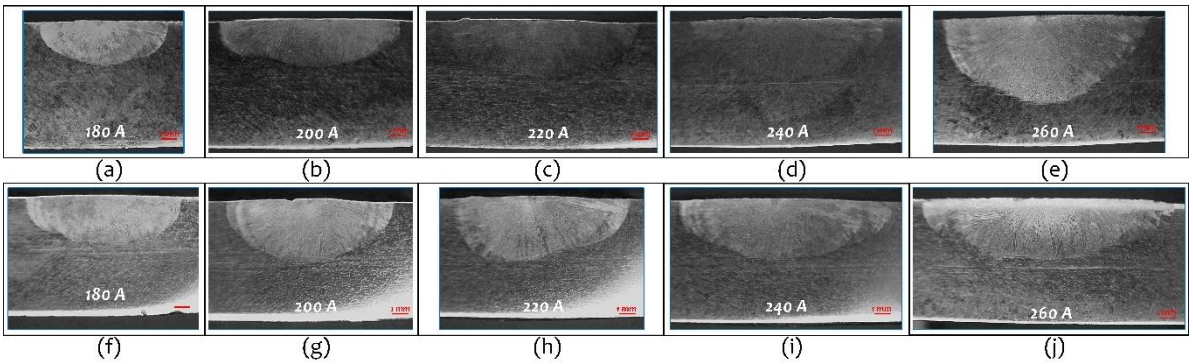


Figure 7.3 : Macrostructure observed for bead-on-plate (Incoloy 800HT) welds (a-e) with SiO_2 flux (f-j) with TiO_2 flux

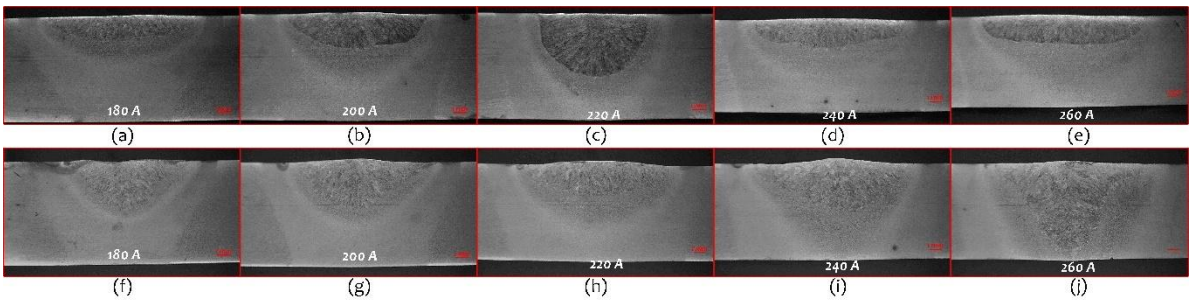


Figure 7.4 : Macrostructure observed for bead-on-plate (P91) welds (a-e) with SiO_2 flux (f-j) with TiO_2 flux

Table 7.1 : Weld bead width and depth of penetration of different weld beads obtained

Material	*Flux*	*Weld width/DOP*	*Pass 1 (180 A)*	*Pass 2 (200 A)*	*Pass 3 (220 A)*	*Pass 4 (240 A)*	*Pass 5 (260 A)*
Incoloy 800HT	SiO_2	Weld width (mm)	8.2	11.4	12.5	12.6	13.1
		DOP (mm)	2.8	3.1	3.7	3.9	5.7
	TiO_2	Weld width (mm)	10.7	10.8	11.4	13.4	16.2
		DOP (mm)	3.3	4.4	4.6	4.1	4.1
P91	SiO_2	Weld width (mm)	11.5	11	8.6	13.3	14.2
		DOP (mm)	1.72	2.8	4.8	2.7	2.5
	TiO_2	Weld width (mm)	10	11.7	12.2	12.3	13.6
		DOP (mm)	3.9	3.9	3.5	4.2	8.1

The performed bead-on plate weld helps the observe that TiO_2 flux gave a maximum depth of penetration of up to 8 mm in the P91 plate while SiO_2 flux gave a maximum depth of penetration of up to 5.7 mm in the Incoloy 800HT plate. Interestingly, TiO_2 flux gave an optimum penetration of 4.6 mm in Incoloy 800HT at 220 A, and only at 220 A optimum penetration of 4.8 mm was observed in the P91 plate using SiO_2 flux. This result can be utilized to design an optimized dual-component flux for future work to weld P91 or Incoloy 800HT. Also, the obtained data can be used to perform a dissimilar metal weld between P91 and Incoloy 800HT.

7.2 P91 SIMILAR WELDED JOINT USING A-TIG WELDING TECHNIQUE

7.2.1 Macroscopic Observations

The welding was performed on a special purpose semi-automatic welding table. The copper backing plate was also installed to achieve a stable welding arc (Figure 7.5(a)). The flux paste prepared with methanol was applied on the faying surface prior to welding, as shown in Figure 7.5(b). The final welded plate (Figure 7.5(c)) had a uniform weld bead with uniform and complete penetration. The cavity at the starting point and weld bead shape in the macrograph (Figure 7.5(d)) confirms the reversal of Marangoni flow.

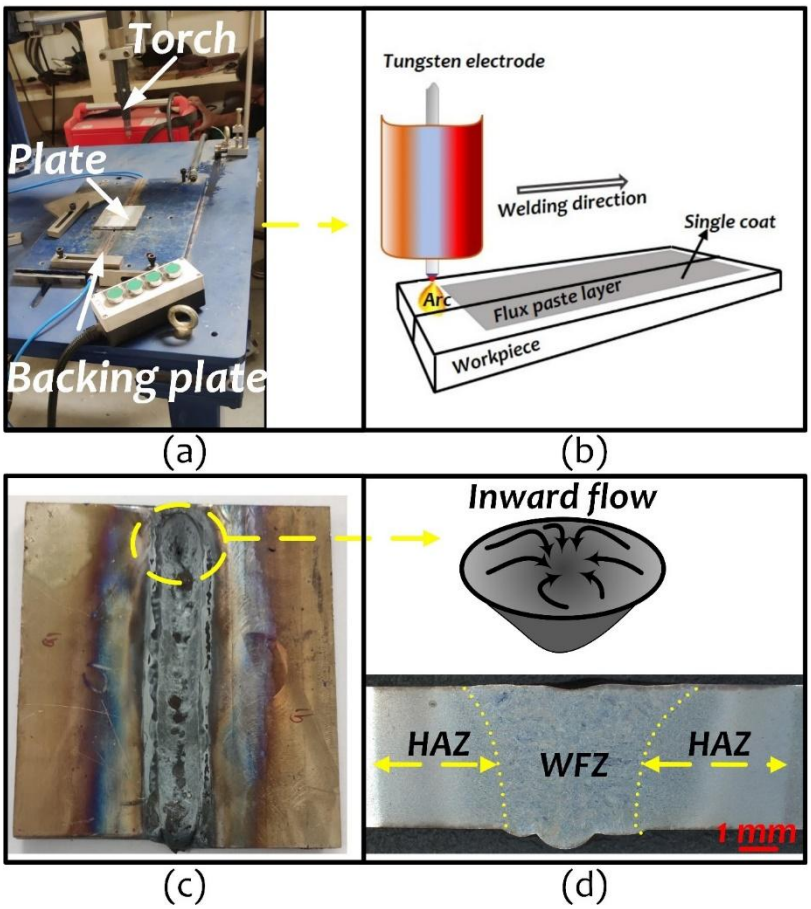


Figure 7.5 : (a) A-TIG welding setup; (b) welding process schematic; (c) welded plate; (d) weld macrograph

7.2.2 Heat Affected Zone (HAZ) Microstructure Characterization

Various precipitates, such as carbides, nitrides, and intermetallic phases, can potentially develop in P91. The development and progression of these phases are significantly impacted by the thermal exposure and duration of exposure to elevated temperatures. The evolution of precipitates during high-temperature processing and service is a crucial determinant of the microstructure and properties of P91 (Sirohi et al., 2020). A sequence of temperature ranges can characterize the development of precipitates in P91. The initial nucleation occurs within a temperature range of 550-650 °C. This results in the production of carbides within the matrix. The phenomenon of precipitate growth is observed within a temperature range of 650-750 °C, during which the carbides undergo further growth and agglomeration. The phenomenon of coarsening occurs within the temperature range of 750-900 °C, during which the carbide clusters increase in size and merge to form larger particles. The phenomenon of dissolution takes place at temperatures exceeding 900 °C, whereby the carbides undergo dissolution, and the steel matrix undergoes a transformation into an austenitic phase. The alteration of these solid particles can exert a noteworthy influence on the physical characteristics of P91, particularly under elevated thermal

conditions (Kimura et al., 2009; Lolla et al., 2014). The occurrence of sizable carbide particles may result in reduced toughness and heightened vulnerability to cracking while welding. Therefore, it is vital to understand the precipitation evolution in P91 to improve the processing and service conditions, which will ultimately lead to achieving the ideal microstructure and mechanical properties. The HAZ regions that formed near both weld interfaces were of paramount interest for the P91 weld. The average widths of the HAZ on both sides were identical, and there were no notable differences noted between the two sides. It is possible to make out, as depicted in Figure 7.6, the creation of several HAZ zones as a function of temperature change. In the CGHAZ region, the specimen representing the AW condition was spotted quite close to the weld interface. The CGHAZ area had been subjected to temperatures greater than the A_{c3} transformation temperature, which resulted in the creation of grains with a big size. Because of the extremely high temperatures, a large amount of the precipitates were dissolved into the matrix, and as a result, the CGHAZ was found to have the fewest quantity of precipitates. The grain size observed in the CGHAZ was around 25 ± 5 µm. The FGHAZ region was seen to be located right next to the CGHAZ region. It was exposed to the heat to a level that was almost exactly equal to the A_{c3} transition temperature. As a result of a lower percentage of precipitate removal, FGHAZ was found to have limited grain development, which caused grain borders to get pinned. The grain size observed in the FGHAZ was around 8 ± 5 µm. Further, ICHAZ was observed in a very thin region. ICHAZ is formed in the region exposed to the transformation temperature between A_{c1} and A_{c3}. The grain size observed in the FGHAZ was around 12 ± 5 µm. ICHAZ region also had the presence of over-tempered martensite (Pandey et al., 2018c).

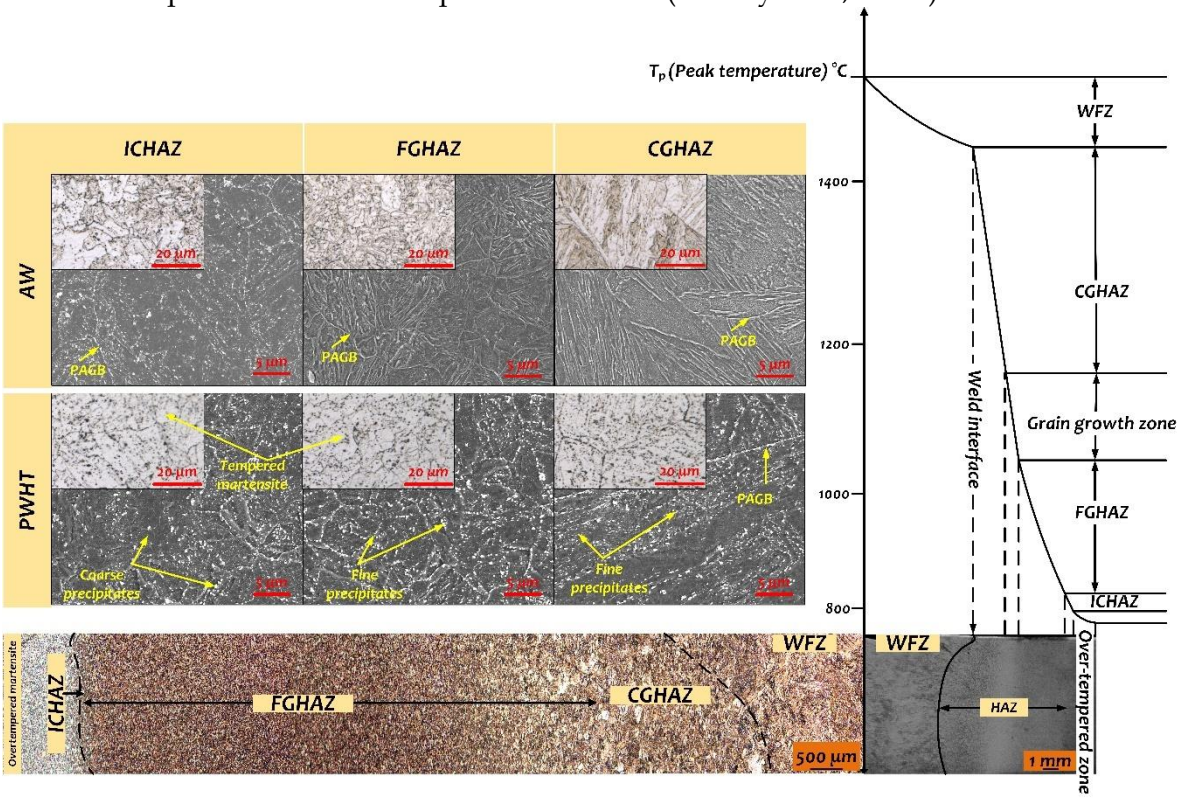


Figure 7.6 : Detailed visualization of different HAZ regions formed after exposure to different transformation temperatures

During the process of welding, the increased temperature causes the carbides and MX precipitates that are contained inside the austenitic matrix to dissolve. Hence, the P91 weld underwent a post-weld heat treatment that was characterized by the precipitation and development of $M_{23}C_6$ carbides and MX precipitates. Figure 7.6 illustrates the changes that occurred in the various HAZ zones as a result of PWHT. Carbide and MX precipitates become less soluble due to an increase in the concentration of alloying elements that occurs

due to the cooling process. The cooling process causes this decrease in solubility. The precipitation of these elements is brought about as a result of the decrease in their solubility. The precise temperature values and duration of heat treatment are crucial factors that dictate the magnitude and dispersion of the precipitates.

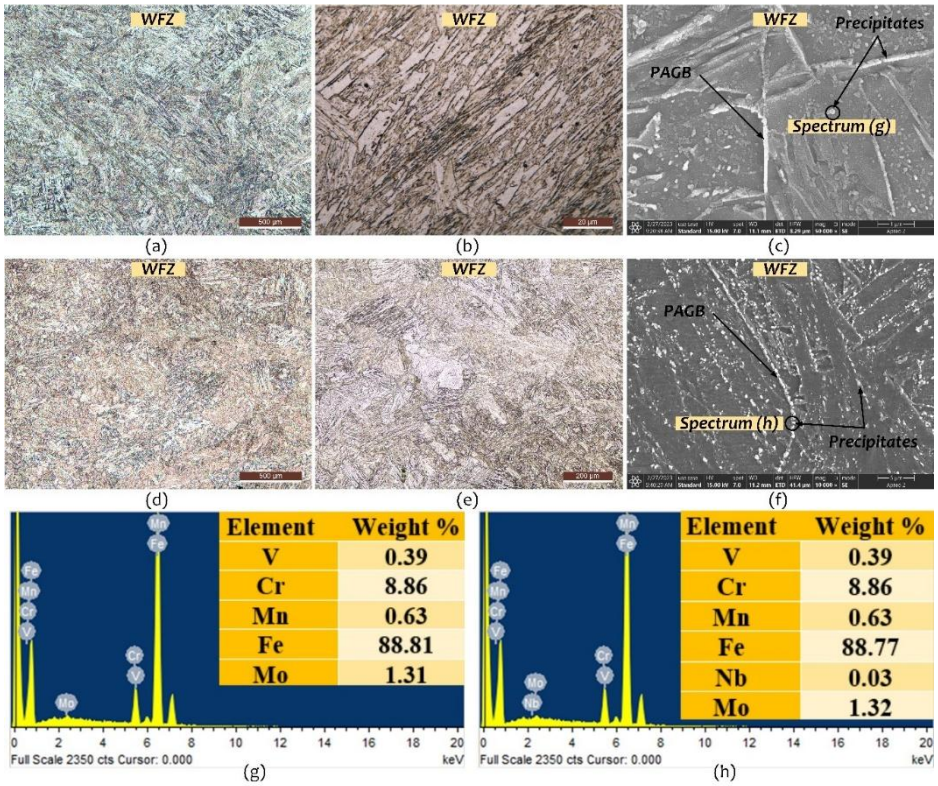


Figure 7.7 : Micrographs of (a) AW state WFZ at lower magnification (b) AW state WFZ at higher magnification (c) AW state WFZ under FE-SEM (d) PWHT state WFZ at lower magnification (e) PWHT state WFZ at higher magnification (f) PWHT state WFZ under FE-SEM (g) EDS spectrum of precipitate observed in AW state WFZ (h) EDS spectrum of precipitate observed in PWHT state WFZ

7.2.3 Weld Interface and Weld Fusion Zone (WFZ) Microstructure Characterization

The solidification mechanics of P91 steel during welding are intricate and can be impacted by multiple factors, such as the welding methodology employed, the P91 steel composition, and the cooling rate during the solidification process. The solidification process involves the gradual cooling of the molten metal in the weld pool, forming a solidified structure commonly referred to as the weld bead. During the cooling process, a distinct interface is established between the solid and liquid areas of the weld bead. The present interface exhibits dynamic characteristics and is capable of undergoing movement while undergoing the process of solidification. The solidification mechanism of P91 steel can be altered by the inclusion of alloying elements, such as chromium and molybdenum (Zhang, 2009). These elements could create intricate intermetallic compounds with other constituents present in the steel. The compounds have the potential to influence the kinetics of solidification, thereby resulting in the development of distinct microstructural features within the weld bead. The presence of a diverse array of intermetallic phases, such as $M_{23}C_6$ carbides, MX carbonitrides, and Laves phases, has been detected in P91 welds. These phases can exert a notable influence on the mechanical characteristics of the weld. Rapid cooling rates can facilitate the promotion of fine-grained microstructures with enhanced toughness, whereas slower cooling rates can result in the formation of coarse-grained microstructures with diminished toughness. As per the findings of a study conducted by (Zhang, 2009), elevating the cooling rate during P91 welding led to the development of a more refined microstructure, resulting in enhanced hardness and tensile strength. The solidification

mechanism of P91 is contingent upon a multitude of factors, including but not limited to the welding methodology, rate of cooling, and composition of the alloy.

P91 steel's WFZ predominantly undergoes a martensitic transformation during the solidification. During the cooling stage of the welding process for P91 steel, the material goes through a transition that produces a martensitic structure. The fast-cooling rates that are inherent to the welding process are the cause of this quick transformation. The solidification mode influences the microstructure and mechanical properties of the P91 weld. The selection of the flux composition is crucial as it can significantly affect the quality and properties of the weld. It is imperative to optimize the welding parameters to attain adequate penetration and fusion while avoiding excessive heat input that may compromise the weld's quality or result in HAZ's cracking. The WFZ microstructure, as observed in Figure 7.7(a-b), the WFZ in AW state had extensive growth of martensitic grains. The lath block boundaries and PAGBs in WFZ were observed with the presence of precipitates over them, as shown in Figure 7.7(c). Precipitates were observed in the WFZ in the AW state, but the precipitate density increased significantly after PWHT. The optical micrograph of the WFZ after PWHT at different magnifications was noticed with no significant change in grain size, as shown in Figure 7.7(d-e), and heavy fresh precipitation can be observed in Figure 7.7(f). The EDS spectrum shown in Figure 7.7(g-h) for the precipitates observed in the WFZ concludes the possible presence of Cr and Mo-rich phases. The utilization of flux coating has been observed to enhance the microstructural properties by mitigating unfavorable phase formation and facilitating structure formation. A comparative analysis was conducted in a particular study to evaluate the microstructural properties of P91 welds that were generated through the utilization of flux coatings made of aluminum oxide and titanium oxide.

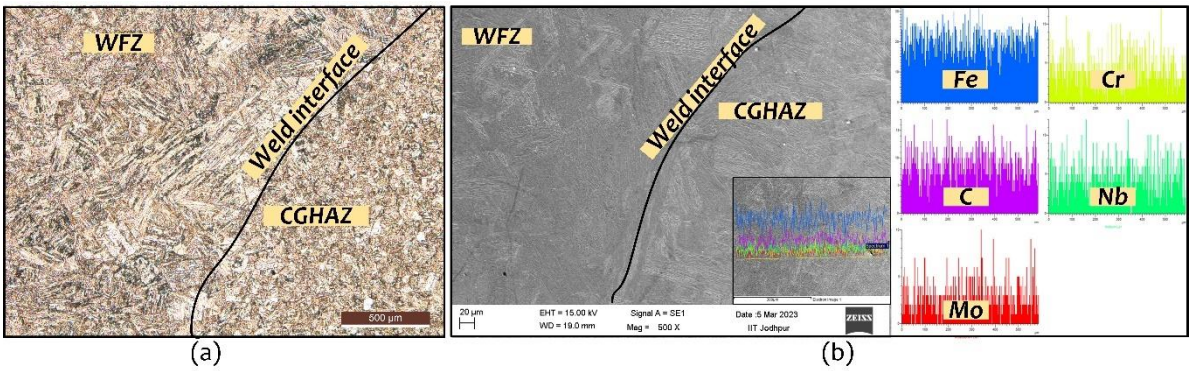


Figure 7.8 : Micrograph of weld interface (a) under an optical microscope (b) in FESEM with line map spectra

Microsegregation is a prevalent occurrence that may transpire during the welding process of P91 steel. This phenomenon results in the development of distinct areas with varying chemical compositions, potentially compromising the weld joint's mechanical characteristics. Numerous scholarly inquiries have explored the microsegregation phenomena in P91 welds, and specific approaches have been suggested to alleviate its impacts. (Zhang, 2009) conducted a study to examine the microsegregation behavior in P91 welds across different welding conditions, encompassing diverse heat inputs and cooling rates. The study findings indicate that the microsegregation phenomenon was impacted by heat input and cooling rate. Specifically, greater heat inputs were associated with heightened microsegregation severity, while faster cooling rates were linked to a more homogeneous chemical composition. (Jabar et al., 2021) conducted a study in which they suggested a technique to alleviate the microsegregation consequences through the introduction of a minor quantity of niobium into the weld material. The findings indicate that the inclusion of niobium led to a significant reduction in microsegregation within the WFZ, resulting in

enhanced mechanical characteristics of the welded joint. (Vimalan et al., 2017) conducted a study to examine the impact of PWHT on microsegregation behavior in P91 welds. The findings indicate that PWHT can effectively mitigate microsegregation, thereby enhancing the mechanical characteristics of the welded connection (Santella et al., 2010; Shibli, 2017).

The optical micrograph of the P91 weld interface in Figure 7.8(a) shows that the weld interface can be distinguished based on grain shape and size only, and it is difficult to recognize any distinct weld interface. The martensitic grain growth at the interface was not particularly perpendicular, but lath packets and grain groups were observed to be aligned in a similar direction along the weld interface and WFZ. The micrograph in Figure 7.8(b) shows an EDS line map across the weld interface, and no significant diffusion or microsegregation was observed. The distribution of alloying elements was mainly constant across the weld interface. The impact of flux coatings on the diffusion and microsegregation of alloying elements in P91 welds can be altered by using activated TIG welding. The flux coating can influence the distribution of alloying elements during solidification and the resulting microstructure and mechanical properties of welds. Research has been conducted to examine the impact of various fluxes on the diffusion and microsegregation of alloying elements in P91 welds. An investigation was conducted to examine the impact of flux coatings containing aluminum oxide and titanium oxide on the dispersion of alloying elements in P91 welds (Pandya et al., 2021; Singh et al., 2017). The study's findings indicate that the utilization of flux coatings resulted in a decrease in the diffusion and microsegregation of alloying elements, leading to a more uniform dispersion of alloying elements across the welds.

7.2.4 Tensile Properties

The evaluation of the tensile characteristics of P91 welds is crucial in guaranteeing the robustness and longevity of the welded joint. P91 steel is a type of steel that exhibits high temperature (HT) strength due to the presence of chromium, molybdenum, and vanadium (Pandey et al., 2018d). These elements contribute to the steel's exceptional resistance to corrosion and ability to withstand high temperatures. The prepared tensile specimens and their fractured locations are shown in Figure 7.9. In AW condition, the flat room temperature standard specimen failed from the base metal after elongation of 17%, giving UTS of 779 ± 10 MPa. After PWHT, the UTS dropped to 700 ± 10 MPa. The process of PWHT is of utmost importance in attaining the intended tensile characteristics of the welded joint. Proper execution of the PWHT results in a P91 weld joint that exhibits elevated tensile strength and elongation levels (Pandey et al., 2018e). After, PWHT elongation increased up to 23%, suggesting PWHT introduced ductility as the reduction in the area also increased by 9%. However, after PWHT, the specimen was observed to fail from the FGHAZ, which could be due to the detrimental effects of precipitate coarsening as it will act as a nucleation site for the void. The fine-grain martensitic transformation in the FGHAZ region is attributed to local strain distribution. Though type IV long-term exposure is unlikely here, the weak sloid solution strengthening of FGHAZ due to partial dissolution may have played an important role. The sub-size specimen was tested to determine the strength of the WFZ. In the AW state, the UTS was a maximum of 863 ± 10 MPa, but sudden failure was observed due to the very brittle nature of the WFZ. PWHT successfully imparted ductility to the WFZ, and a UTS of 732 ± 10 MPa was observed with an 18.75% increase in elongation percentage.

Further HT tensile tests were also conducted to observe the strength of the weld at elevated service temperatures. The engineering stress-strain curves for tested specimens are shown in Figure 7.9. Table 7.2 summarizes the test data obtained for the tested specimens. The round HT-tensile specimen tested at 450 ˚C gave the UTS of 512 ± 10 MPa, and the reduction in the area was around 40%, and the specimen failed from the base metal. At the

maximum operating temperature of P91, i.e., 550 ˚C, the UTS decreased to 469 ± 10 MPa, showing a slightly high elongation percentage and failure occurred in the base metal.

The fractography of the AW state in Figure 7.10(a) shows a completely ductile mode of failure in the base metal with the presence of dimples and precipitates. The fractography of the PWHT standard specimen in Figure 7.10(b) failing from FGHAZ shows the fractured surface with dimples indicating ductile failure. The formation of tear ridges can be observed in Figure 7.10(c), showing the AW subsize fracture surface. The presence of a mixed mode of failure can be observed with fewer dimples and cleavage facets. Tear ridges were also observed, and an overall brittle fracture mode was observed. Figure 7.10(d) shows a highly ductile failure mode in WFZ of a PWHT subsize specimen, attributing to fresh fine precipitates. The HT tensile specimen fractography shown in Figure 7.10(e) for 450 ˚C and Figure 7.10(f) for 550 ˚C shows a completely ductile failure mode. HT tensile specimens show a clear formation of cups and cones. The fractured is uniformly distributed with dimples of uniform size. Voids and precipitates were also visible on the fractured surface. Also, the presence of shear lips shows the during ductile mode of failure, it absorbed energy through plastic flow.

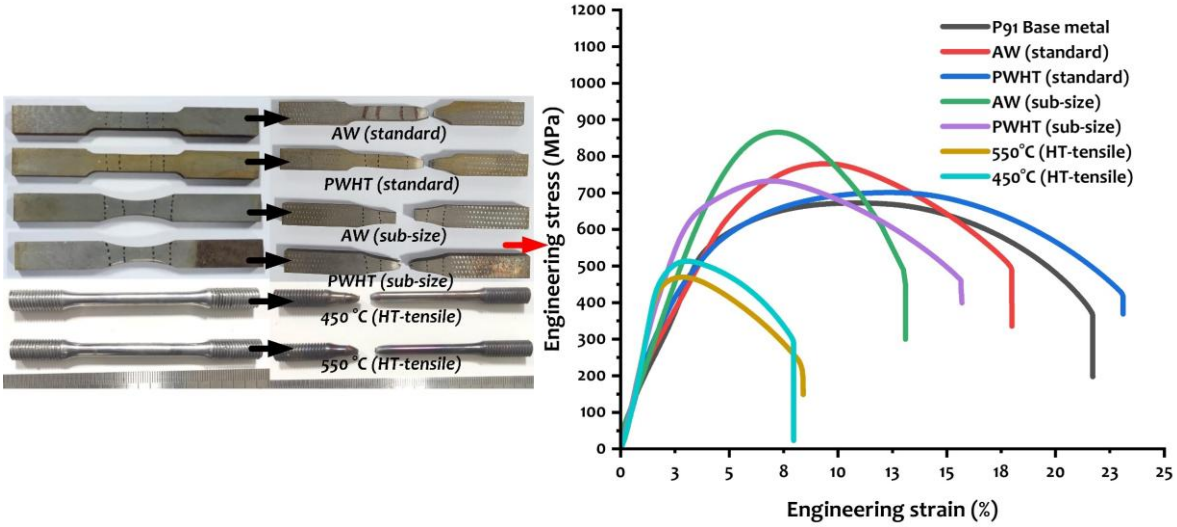


Figure 7.9 : Room temperature flat tensile specimens and high temperature (HT) round specimens under tensile loading with the engineering stress-strain curves for the tested specimens

Table 7.2 : Tensile properties

Specimens	*UTS (MPa)*	*YS [offset 0.2%] (MPa)*	*Elongation (%)*	*Reduction in the area (%)*	*Failure site*
AW (Standard flat specimen)	779 ± 10	338 ± 10	18 ± 1	21 ± 1	Base metal
PWHT (Standard flat specimen)	700 ± 10	364 ± 10	23 ± 1	30 ± 1	FGHAZ
AW (Subsize flat specimen)	863 ± 10	-	13 ± 1	2 ± 1	WFZ
PWHT (Subsize flat specimen)	732 ± 10	-	16 ± 1	24 ± 1	WFZ
450 ℃ (Round specimen)	512 ± 10	-	8 ± 1	38 ± 1	Base meta
550 ℃ (Round specimen)	469 ± 10	-	9 ± 1	40 ± 1	Base metal

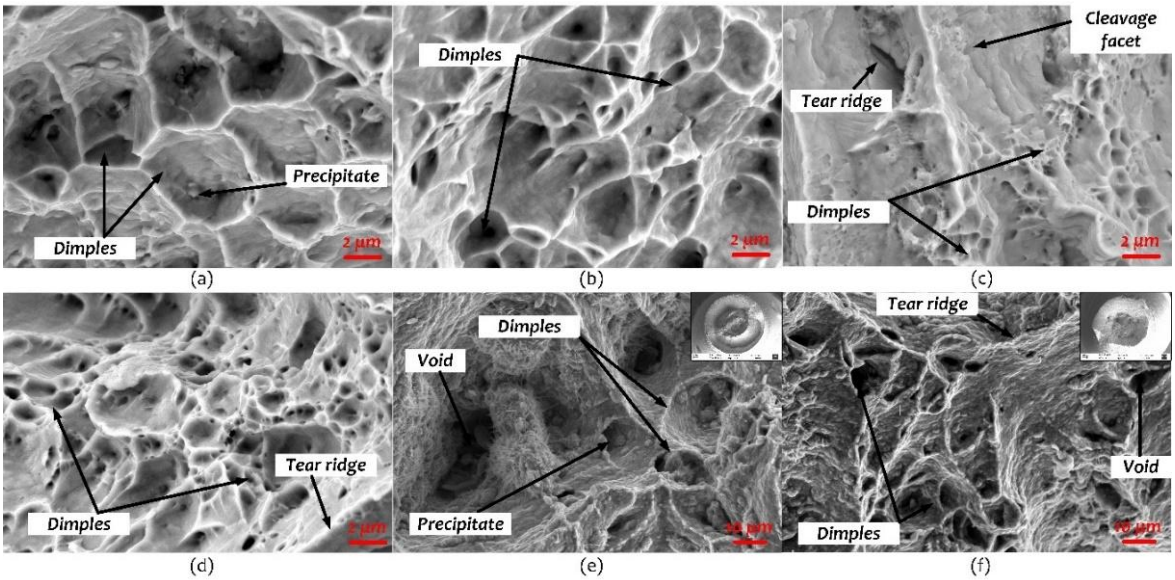


Figure 7.10 : Fractography micrographs of (a) AW state standard specimen (b) PWHT state standard specimen (c) AW state sub-size specimen (d) PWHT state sub-size specimen (e) HT-tensile specimen at 450 °C (f) HT-tensile specimen at 550 °C

7.2.5 Microhardness Properties

The correlation between the microstructure and hardness of P91 welds is significant, as the hardness is contingent upon the microstructural characteristics evident in the weld. The constituents present in P91 welds' microstructure comprise tempered martensite and carbides. The formation of said constituents results from welding, whereby the weld undergoes rapid cooling after exposure to elevated temperatures. The microstructural characteristics, specifically the quantity and arrangement of carbides, are the primary factors that impact the hardness of P91 welds. The P91 base metal in the normalized and tempered state had an average microhardness of 245 ± 5 HV. The dissolved precipitates in WFZ and CGHAZ in the AW state strengthen the solid solution and increase microhardness. The Nb-rich precipitates remain undissolved and hinder dislocations, providing strength and hardness in the region. Hence, in the AW state, the CGHAZ region was observed with a maximum microhardness of 450 ± 5 HV and WFZ 460 ± 5 HV. Hardness increases as carbon and nitrogen dissolve in a matrix. The introduction of carbon (C) and nitrogen (N) atoms into the crystal lattice could have impeded the movement of dislocations. The minimum value of 422 ± 5 HV was observed in the WFZ. The microhardness variation plot for AW and PWHT state specimens is shown in Figure 7.11.

The weld interface showed a dropped microhardness of a minimum of 397 ± 5 HV. The possible lowest microhardness in the ICHAZ region was 205 HV. The average microhardness in the over-tempered region was 219 ± 5 HV. In the FGHAZ region, microhardness gradually decreased from 440 ± 5 HV to 301 ± 5 HV. After PWHT, the average microhardness of 265 ± 20 HV was observed in the WFZ and HAZ regions. The microhardness near the completely tempered ICHAZ region after the PWHT was 210 HV. After PWHT, the enhancement of mechanical properties can be attributed to more significant and more homogeneously dispersed precipitates. The formation of these precipitates impedes the motion of dislocations, thereby enhancing the material's mechanical properties in terms of strength and toughness. Furthermore, the application of heat treatment has the potential to decrease residual stresses and enhance the microstructural characteristics of the weld. The observed microhardness is comparatively higher than the reported studies (Maduraimuthu et al., 2012; Vidyarthy and Dwivedi, 2018) with different settings, possibly due to high heat input.

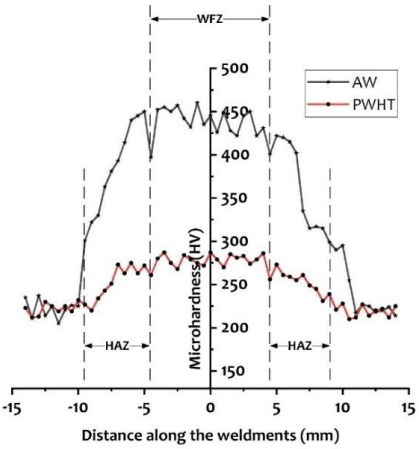


Figure 7.11 : Microhardness variation plot across the P91 WFZ for AW and PWHT specimens

7.2.6 Charpy Impact Toughness

The Charpy impact toughness characteristics of P91 welds are paramount in guaranteeing the weld's ability to withstand fracture and crack propagation when subjected to dynamic loading circumstances. The AW specimen had a Charpy impact toughness of 76 ± 15 Joules; in the PWHT state, it was 98 ± 15 Joules. After PWHT, the tempering of martensite and precipitation of fine $M_{23}C_6$ precipitates may have contributed to the increase in toughness. The fractography micrograph in Figure 7.12(a) shows a brittle failure mode with large cleavage facets and tear ridges. The weld joint qualifies the minimum toughness criteria laid by the European specification EN 1599:1997. Figure 7.12(b) shows a slight presence of dimples in the PWHT specimen, confirming the slight increase in toughness after PWHT. However, the mode of failure in WFZ was mixed. Several research studies have examined the Charpy impact toughness characteristics of P91 welds with varying welding conditions and PWHT. (Pandya et al., 2021) conducted a study to examine the impact of varying PWHT temperatures on the Charpy impact toughness characteristics of P91 welds. The findings indicate that the Charpy impact toughness of the weld joint exhibited an upward trend as the PWHT temperature was raised, with the highest value being attained at 760 °C. (Arivazhagan and Vasudevan, 2014) conducted a study to examine the impact of various welding parameters on the Charpy impact toughness characteristics of P91 welds. The findings indicate that augmenting the heat input during the welding process reduced the Charpy impact toughness of the welded joint.

Furthermore, it was observed that a synergistic effect of elevated welding temperature and PWHT enhanced the Charpy impact toughness characteristics. The process of PWHT has the potential to induce carbide precipitation within the microstructure of the weld. This occurrence has been observed to enhance the weld's resistance to creep and improve its toughness. Carbide formation is a consequence of the diffusion of carbon and other alloying elements that occurs during heat treatment.

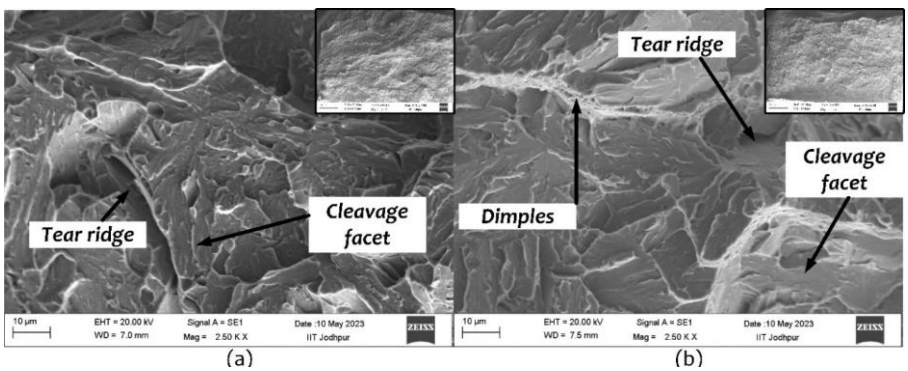


Figure 7.12 : Fractography micrograph of (a) AW state Charpy impact toughness specimen; (b) PWHT state Charpy impact toughness specimen

7.3 INCOLOY 800HT SIMILAR WELDED JOINT USING A-TIG WELDING TECHNIQUE

7.3.1 Macroscopic Observations

The welded plate in Figure 7.13(a) shows a uniform weld bead, and complete penetration can be confirmed from the macrograph in Figure 7.13(b). The preliminary observation of the weld fusion zone, weld interface, and HAZ is shown in Figure 7.13(b). The HAZ formation is not distinctive, but the average grain size observed near the weld interface was 172 ± 12 μm. The austenitic grains in the HAZ were slightly resolved into the WFZ. The weld interface was also observed with a very thin partially mixed zone (PMZ) formation. PMZ is formed due to partial melting of the base metal near the weld interface as it is exposed to a temperature ranging between the liquidus and non-equilibrium solidus temperature of Incoloy 800HT base metal (Taheri et al., 2017). The growth at the weld interface was columnar, and cellular dendritic growth was also witnessed as it progressed to the center of the WFZ. The weld top region and center have equiaxed dendritic growth due to the very high rate of cooling of the weld pool. The Incoloy 800HT weld during solidification transforms as Liquidus → Liquidus + γ → Liquidus + γ + TiC → γ + TiC (DuPont, 2009). Hence, the weld solidification mode is completely austenitic. The HAZ region of Incoloy 800HT was not witnessed with any particular thinking of the austenitic grain boundaries as discussed for previous different DWJs. The grain size observed in the Incoloy 800HT HAZ was around 175 ± 10 μm

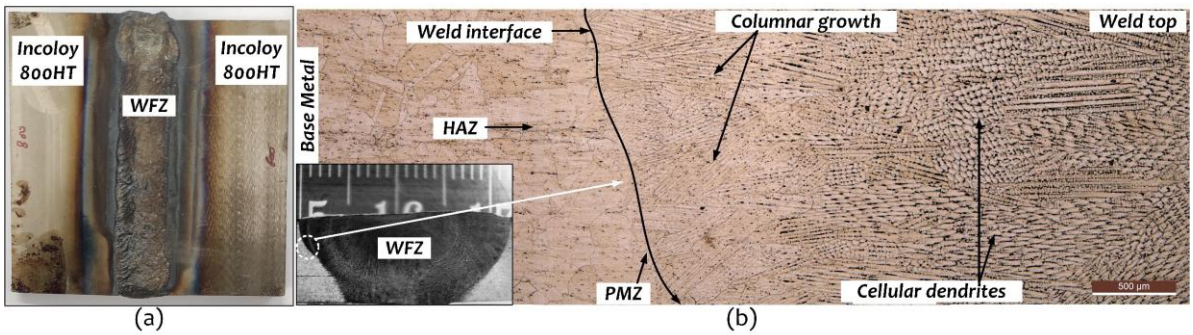


Figure 7.13 : A-TIG welded plate and weld bead macrograph with stitched optical micrograph of Incoloy 800HT weld

7.3.2 Weld Interface and Weld Fusion Zone (WFZ) Microstructure Characterization

In the presented A-TIG weld interface (Figure 7.14), the PMZ was spotted in very narrow and localized zones. The reduction in PMZ formation could be attributed to the single-pass A-TIG welding process. The weld interface was found to be heavily precipitated with Ti and Nb-based precipitates and different carbides. Figure 7.14 shows the line map EDS across the weld interface. No major variation in elemental distribution across the weld could be witnessed. The lack of diffusion across the weld interface could be due to the high solidification rate of the molten weld pool. Few peaks of Ti and C-rich phases suggest the presence of such phases at the weld interface.

The WFZ experienced high cooling rates, which in turn caused competitive growth of dendritic structures. These dendritic structures were separated by solidification subgrain boundaries (SSGBs) (Dak and Pandey, 2020). SSGBs are the last to solidify. These dendritic structures, such as columnar, cellular, and equiaxed, were in groups or packets, and these packets formed Solidification grain boundaries (SGBs) (Dak and Pandey, 2020). Redistribution of solutes occurs at SGBs, and they are prone to the formation of detrimental phases due to high solute concentration over them. Figure 7.15 shows the area map EDS at a located SGB. Heavy deposition of Ti was witnessed over it. A slight percentage of C and Nb was also there in the same region. The vigorous growth of dendrites at the end of weld solidification stages, notably in the center of WFZ, the high angle misorientation SGB

migrates and intersects the dendrites to form the migrated grain boundaries (MGB) (Galler et al., 2016), as observed in Figure 7.15.

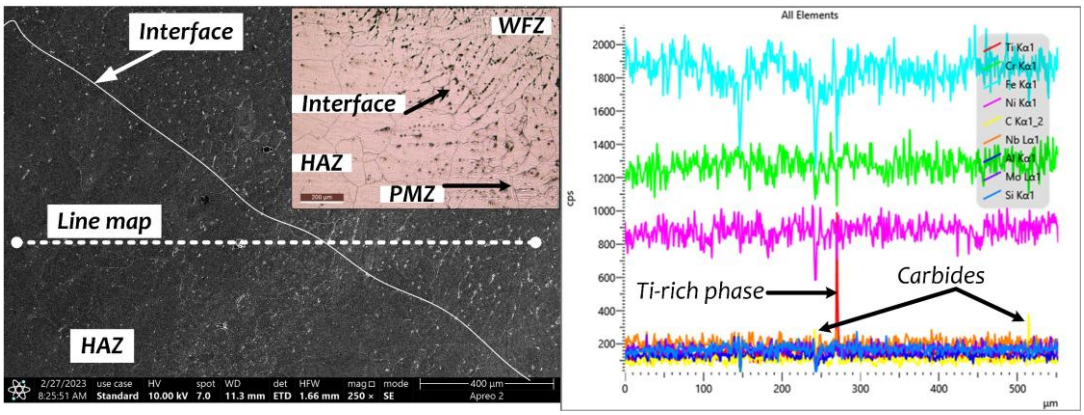


Figure 7.14 : Micrograph of Incoloy 800HT weld interface and line map EDS spectrum across the weld interface

Further EPMA scan was performed across the weld interface, as shown in Figure 7.16. The EPMA scan confirms the heavy presence of Ti and C, rich precipitates in the WFZ and HAZ near the weld interface. No microsegregation of C or substitutional elements was observed in the EPMA scan. The elements present, Fe and Cr, have atomic radii similar to that of Ni. Hence, their coefficient of segregation is near to unity 'k'~1. At the same time, the elements with comparative differences in atomic radii, like C, Ti, Nb, and Mo, may have participated in microsegregation. Extensive partitioning of C and Ti must have caused the heavy formation of precipitates over the grain boundaries and matrix (DuPont, 2009).

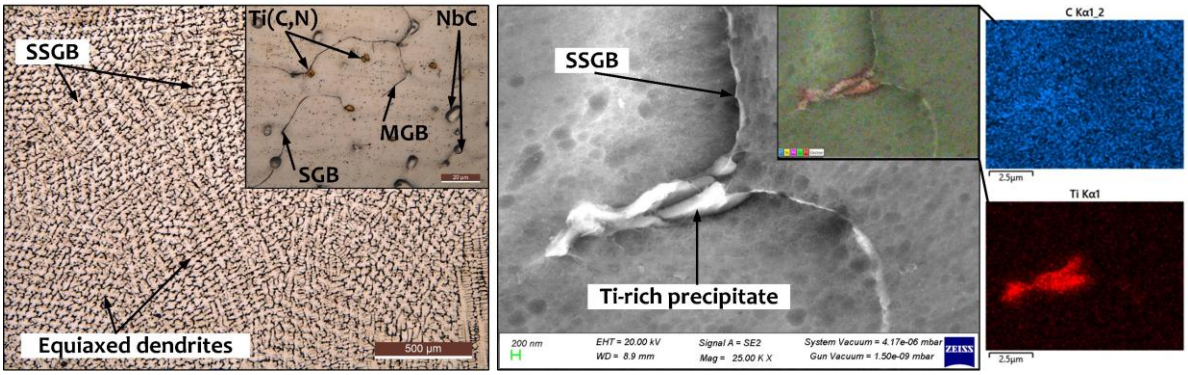


Figure 7.15 : Micrograph of WFZ and area map EDS spectrum over SGB at high magnification

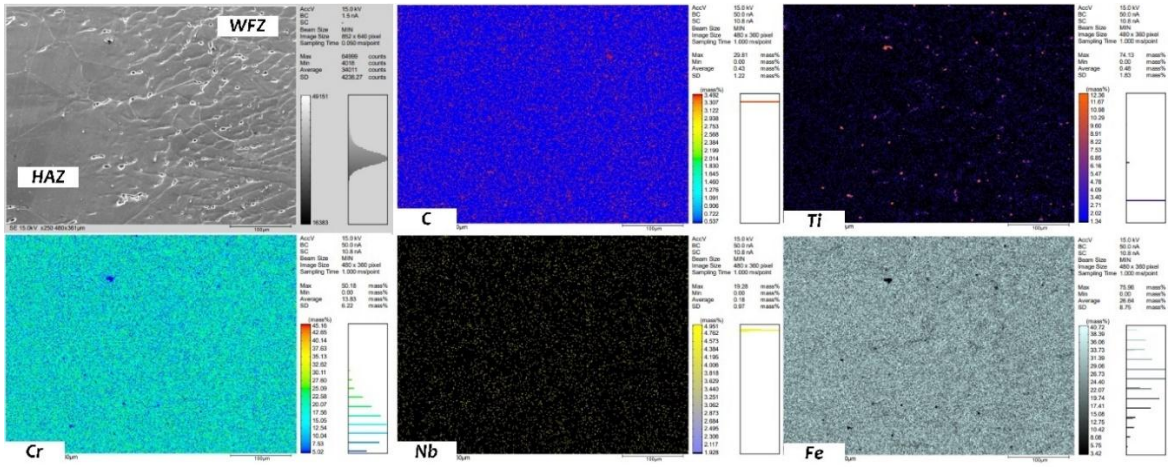


Figure 7.16 : EPMA scan over the Incoloy 800HT weld interface

7.3.3 Tensile Properties

The microstructure properties link to the mechanical behavior of the material. Hence, a detailed characterization of mechanical properties was conducted. The tensile test results are reported in Table 7.3, and the corresponding engineering stress-strain curve can be observed in Figure 7.17(a). The room temperature standard specimen gave the ultimate tensile strength (UTS) of 510 ± 10 MPa and yield strength (YS) of 209 MPa. The specimen failed from the base metal with the highest elongation of 52%, which suggests that the weld had more strength than the base metal. The subsize specimen was also tested at room temperature to estimate the UTS of WFZ, and the observed UTS was 525 ± 10 MPa with elongation at 34%. It suggests that the carbide and Ti-rich precipitates pinned the grain boundaries and improved the strength, and ductility was lost. The fractography of the subsize specimen in Figure 7.17(b) shows the presence of small and large dimples, and tear ridges were also observed. The ductile mode was not as pronounced in the weld as in base metal reported by other authors (Anand et al., 2016; Palanisamy et al., 2021). Precipitates were also visible, suggesting solution hardening and precipitation hardening from the hindrance of dislocation by γ′ phase in the WFZ during weld solidification. Further, a round high-temperature tensile specimen was also tested at 550 ˚C. It gave UTS of 442 ± 10 MPa and elongation of 38%. The YS dropped to 177 MPa. At 650 ˚C, UTS of 366 ± 10 MPa was obtained, and elongation of 26%. The YS dropped to 132 MPa. The flow stress anomaly was witnessed. It was experienced as dislocations glissile in a planar configuration in the initial stage, but when the required thermal activation energy is gained at high temperature, the dislocations turn sessile with a non-planar configuration (Wright et al., 2012). Further microscopic analysis is needed to reason for the loss in elongation percentage.

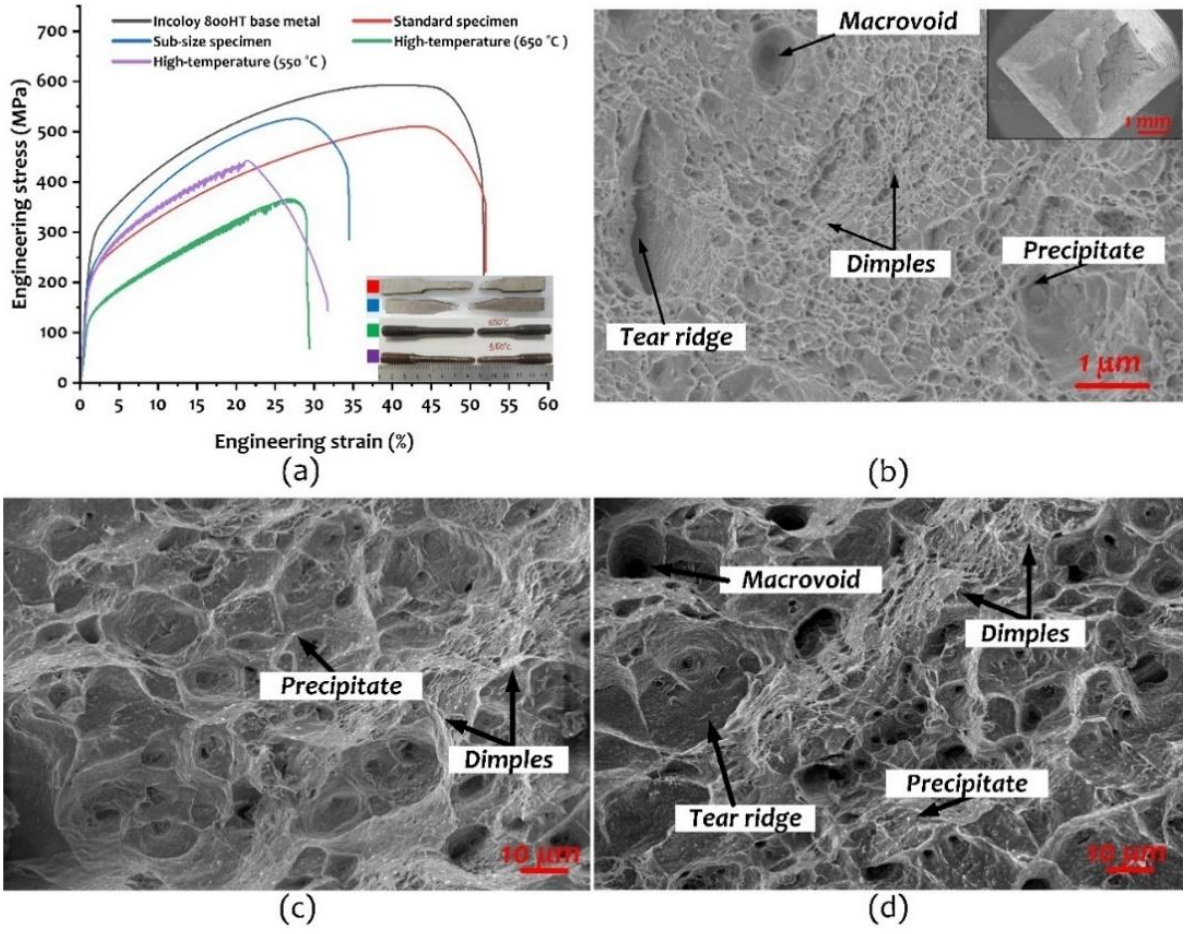


Figure 7.17 : (a) Engineering stress-strain curve and (b) fractography micrograph of fractured WFZ surface (c) HT-tensile specimen at 550 ℃ (d) HT-tensile specimen at 650 ℃

Table 7.3 : Tensile properties

Specimens	*UTS (MPa)*	*YS [offset 0.2%] (MPa)*	*Elongation (%)*	*Reduction in the area (%)*	*Failure site*
AW (Standard flat specimen)	510 ± 10	209	52 ± 1	44 ± 1	Base metal
AW (Subsize flat specimen)	525 ± 10	-	34 ± 1	38 ± 1	WFZ
550 ℃ (Round specimen)	442 ± 10	177	38 ± 1	44 ± 1	Base metal
650 ℃ (Round specimen)	366 ± 10	132	26 ± 1	40 ± 1	WFZ

7.3.4 Microhardness Properties and Charpy Impact Toughness

The microhardness study revealed that WFZ had an average microhardness distribution of 231 ± 10 HV, HAZ region near the weld interface was observed with a slightly low microhardness of 180 ± 10 HV. The peak microhardness observed in WFZ was 235 HV. At last, the base metal had an average microhardness of 175±10 HV. The increase in the microhardness of the WFZ and HAZ region could be attributed to heavy precipitation in WFZ during welding. The Charpy impact toughness of WFZ was also measured to be 97 J, slightly low compared to the 102 Joules of the base metal. This loss in ductility is due to the restriction of dislocation movements due pinning action of the precipitates (Carroll et al., 2010). The variation in microhardness along the weld is represented in the plot shown in Figure 7.18.

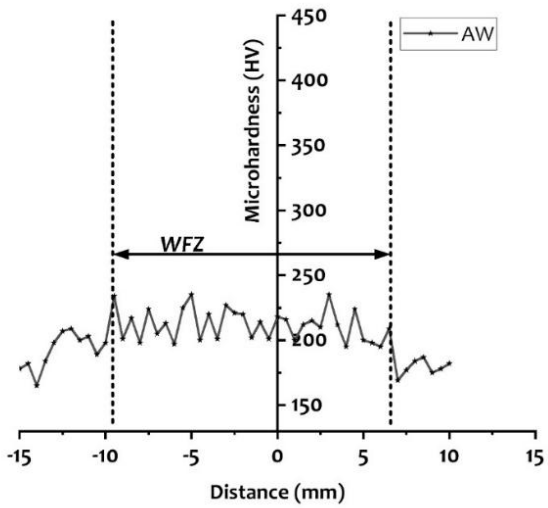


Figure 7.18 : Microhardness variation plot across the weld

7.4 DISSIMILAR WELD JOINT (DWJ) BETWEEN P91 AND INCOLOY 800HT USING A-TIG WELDING TECHNIQUE

7.4.1 Macroscopic Observations

Various flux combinations were tried to achieve complete penetration up to a depth of 8 mm. The initial effect of each flux on the base metals' penetration depth. Then effect of each flux on the depth of penetration on dissimilar welding of the base metals was observed, as shown in Figure 7.19(a-i). There was no arc blow due to the difference in conductivity of the two-base metal. Also, the copper backing plate was used as a precautionary measure. However, the flux that could release more oxygen was observed to form slightly better.

Inspired by these observations and performances, a multicomponent flux (30%TiO_2 + 20%NiO + 20%SiO + 10%V_2O_5 + 5%Cr_2O_3 + 5%MoO_3 + 5%Co_3O_4 + 5%CuO) was finally used. The composition of the multicomponent flux was able to give a complete and uniform DOP for the P91-Incoloy 800HT dissimilar welded joint. As some fluxes could generate more DOP in a specific base metal, a uniform dilution and penetration were obtained from the multicomponent flux. The macroscopic image of the final welded joint is shown in Fig 7.23(j). It shows almost equal dilution from the P91 and Incoloy 800HT base metal. The observations suggest that flux may act differently based on the composition of the base metals, so it becomes necessary to prepare a flux composition such that it affects both the base metals similarly. A-TIG process observes enhanced DOP owing to the two major phenomena. First is the arc constriction phenomenon, which occurs due to the electronegativity of the flux used. The vapors from the flux during welding form an electronegative surrounding around the arc, which pushes the arc radially inwards. A second significant phenomenon in the picture is the reverse Marangoni convection. The Marangoni phenomenon is the surface tension driven action, denoted as thermo-capillary convection. The flux results in the liberation of surface-active element oxygen within the weld pool, thereby altering the surface tension gradient from negative to positive. The phenomenon described involves the movement of molten metal within the weld pool, which is characterized by lower surface tension towards the higher surface tension, specifically the warmer liquid weld pool. The observed flow pattern exhibits an inward direction, starting from the uppermost region of the weld pool and extending toward the center. The major observations from using single component flux were that NiO gave a uniform dilution, while TiO_2 and V_2O_5 gave maximum DOP in the two parent base metals. Co_3O_4 also gave promising DOP and uniform dilution. SiO_2 had a positive effect on the DOP but dilution was more in the P91 base metal. The added cause may be that SiO_2 failed to control the arc blow. MoO_3 responded like SiO_2, but more dilution was observed in the Incoloy 800HT base metal.

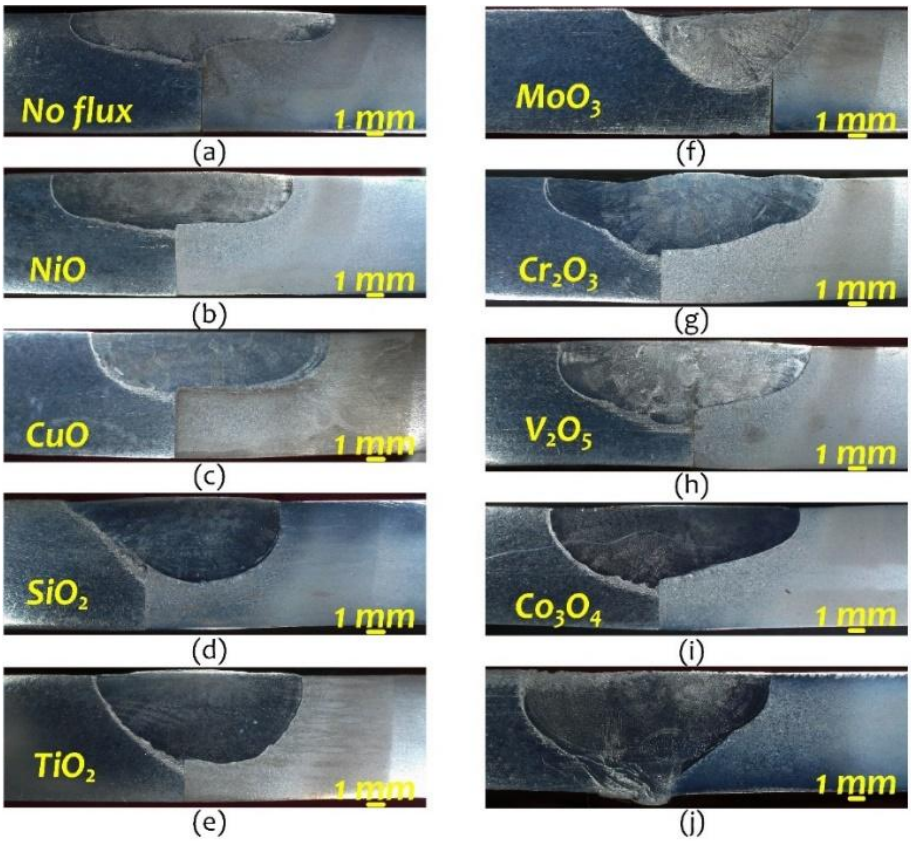


Figure 7.19 : Macrographs of weld beads observed with (a) no flux (b) NiO (c) CuO (d) SiO_2 (e) TiO_2 (f) MoO_3 (g) Cr_2O_3 (h) V_2O_5 (i) Co_3O_4 (j) multicomponent flux

7.4.2 P91 Weld Interface Microstructure Characterization

The microscopic images are arranged in Figure 7.20(a) such that the grain growth at the P91 weld interface and the HAZ formation near it are observed and distinguished. The grain growth in the WFZ was observed cellular substructure (Kumar et al., 2021). The cellular dendritic structure grows from the P91 weld interface inwards to the center of WFZ. Some columnar dendrites were also witnessed near the weld interface region. The weld interface was distinct and continuous, and it was free from any formation of unmixed zones reported as macrosegregation in M-TIG welding (Wang et al., 2021). Though some regions of the weld interface had planar growth, and formation of a Type-II boundary was observed (Lakshmanan et al., 2019). The HAZ region form near the weld interface in the P91 side had the characteristic formation of different zones due to exposure to varying transformational temperatures. The CGHAZ was present near the weld interface with a larger grain size and untempered lath martensite. The grain size gradually decreases over a wide FGHAZ region. The partial dissolution of precipitates restricts the grain growth in the FGHAZ region. The ICHAZ is a thin region found at the end of FGHAZ, with more precipitate density and coarsened precipitates. After ICHAZ region over tempered grains were present in the microstructure. The HAZ region formation has been widely characterized elsewhere. Apart from the width of the HAZ region formation, no distinct feature formation was observed. Hence HAZ region is not characterized further in the present study. Figure 7.20(b) shows the micrograph of the P91 weld interface and elemental variation present across the weld interface region. The elemental mapping shows that WFZ has less Fe concentration and more Cr and Ni concentration, accounting for the austenitic mode of solidification in the WFZ. While Mo is almost uniformly distributed across the weld interface.

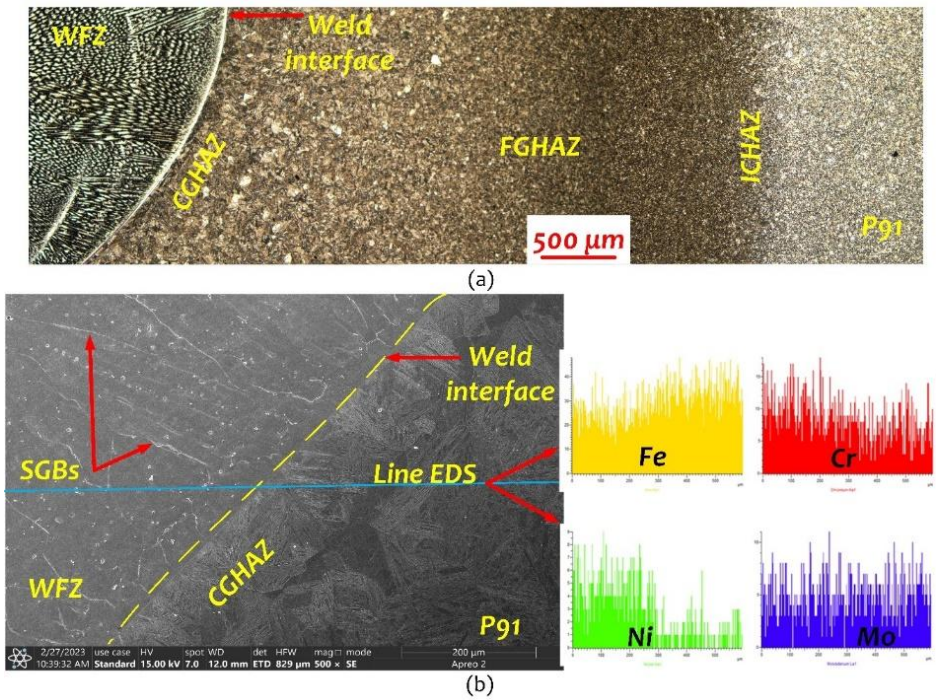


Figure 7.20 : P91 weld interface (a) stitched optical micrograph (b) FESEM micrograph with line mapping

The P91 weld interface in the DWJ was further characterized through the Electron backscatter diffraction (EBSD) technique. Figure 7.21(a) shows an image quality (IQ) map of the P91 weld interface, with contrast distinction at the weld interface. Figure 7.21(b) shows an inverse pole figure (IPF) showing a random orientation of grains in the HAZ region, while in the WFZ, dendrites have grown into packets, and individual packets seem to have a preferred average grain orientation. The grain boundary map in Figure 7.21(c) shows the presence of low angle grain boundaries 1˚-5˚ (LAGBs), medium angle grain boundaries 5˚-

10° (MAGBs), and high angle grain boundaries 15°-180° (HAGBs) (Sayyar et al., 2020; Shamanian et al., 2020; Y. Zhang et al., 2021). The P91 HAZ region dominant the presence of LAGBs and then HAGBs. HAGBs have resulted from the grain growth in the CGHAZ region and the dissolution of Cr-rich precipitates. The major presence of LAGBs assures the mechanical performance of the DWJ. The kernel average misorientation map in Figure 7.21(d) again shows the presence of the high dislocation density in the P91 HAZ region due to thermal stresses experienced during welding. These dislocations in the HAZ region tend to interact with each other, forming a network with the grains and leading to changes in mechanical properties, such as an increase in the microhardness of the region. The phase map (Figure 7.21(e)) shows WFZ near the P91 weld interface being completely fcc due to the austenitic mode of solidification, with a minor presence in the P91 HAZ region just near the interface due to the formation of minor unmixed zones. This also suggests that some martensitic solidification may have occurred at the P91 weld interface. The presence of HAGB near the weld interface also infers that the formation of migrated grain boundaries may have originated from a parent solidified grain boundary in the WFZ (Santella et al., 2002).

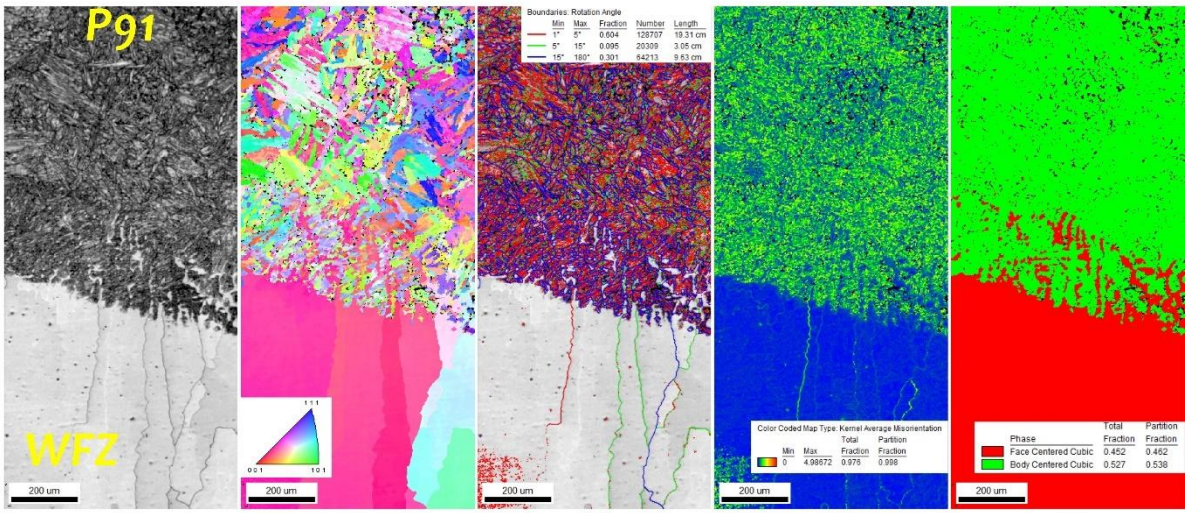


Figure 7.21 : P91 weld interface (a) IQ map (b) IPF map (c) IQ+grain boundary map (d) KAM map (e) phase map

7.4.3 Incoloy 800HT Weld Interface Microstructure Characterization

The Incoloy 800HT weld interface was observed to have a more uniform elemental distribution across the weld interface. The WFZ near the weld interface has a dominant cellular dendritic structure. The Incoloy 800HT HAZ region adjacent to the Incoloy 800HT weld interface had stable austenitic microstructure, as no overall change in the austenitic grain was observed in the HAZ region. The HAZ in Incoloy 800HT DWJ is prone to sensitization and liquation but A-TIG process seems to tackle these defects due to a single TIG pass heat input and thermal stresses were induced. The weld interface was continuous, free from the formation of any unmixed or partially mixed region. The elemental uniformity (Figure 7.22) suggests that the Incoloy 800HT had more dilution and contribution than the WFZ. From the EBSD scan, Figure 7.23(a) shows an IQ micrograph of the Incoloy 800HT weld interface. The IPF map in Figure 7.23(b) shows random orientations of the grain in the Incoloy 800HT HAZ region while the dendritic packets were arranged in a preferred orientation of <100> at the weld interface, suggesting extensive growth of the austenitic grain in some areas of the weld interface. In the grain boundary map in Figure 7.23(c), it is necessary to observe that the significant grain boundaries are HAGBs both in the HAZ region and the WFZ region near the Incoloy 800HT weld interface. HAGBs are familiar to alloys with composition including nickel, chromium, and iron as they have a strong affinity

for a specific crystallographic orientation, which leads to preferential formation of HAGBs during solidification and processing of Incoloy and Inconel alloys. Though HAGBs may act as barriers to grain boundary migration and recrystallization process, they might also promote the segregation of microalloying elements (Sujai and Devendranath Ramkumar, 2020). Figure 7.23(d) shows the KAM map reflection of the presence of dislocation debris in the HAZ grains and grain boundaries, which may be due to the segregation of some microalloying elements such as Ti, C, Nb, and Mo. The phase map in Figure 7.23(e) shows the complete presence of the fcc phase while a very minor fraction of precipitates is bcc. It was observed that columnar grains were growing from the Incoloy 800HT HAZ grain at the interface without any interruptions and had a preferred orientation at the interface. This is because of the competitive mechanism of grain growth, where grains the preferably orientated along the thermal gradient to grow rapidly ("Chapter 1: Weld Solidification," 1997). As a result, fcc grain in the WFZ at the weld interface shows <001> growth direction nearly parallel to the flow direction gradient of the heat (Shin et al., 2018).

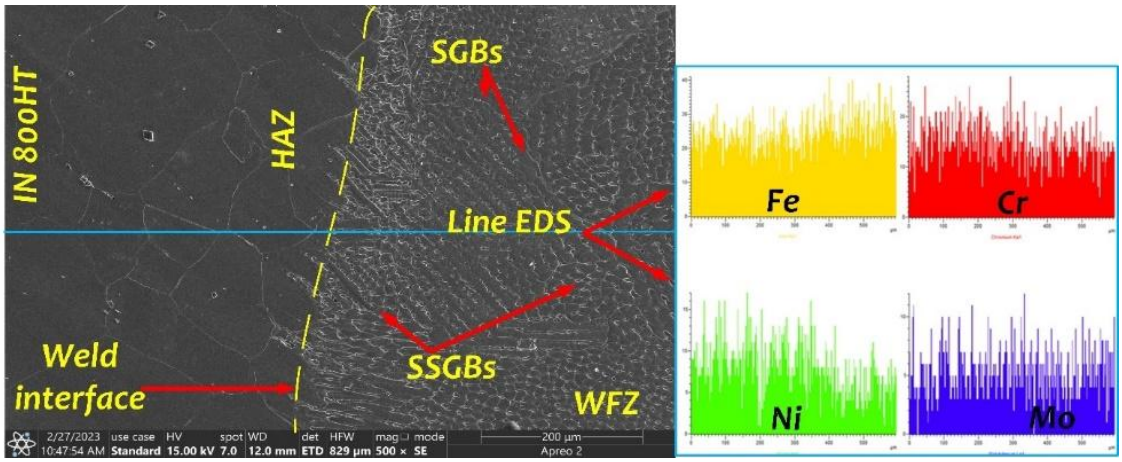


Figure 7.22 : Incoloy 800HT weld interface FESEM micrograph with line mapping

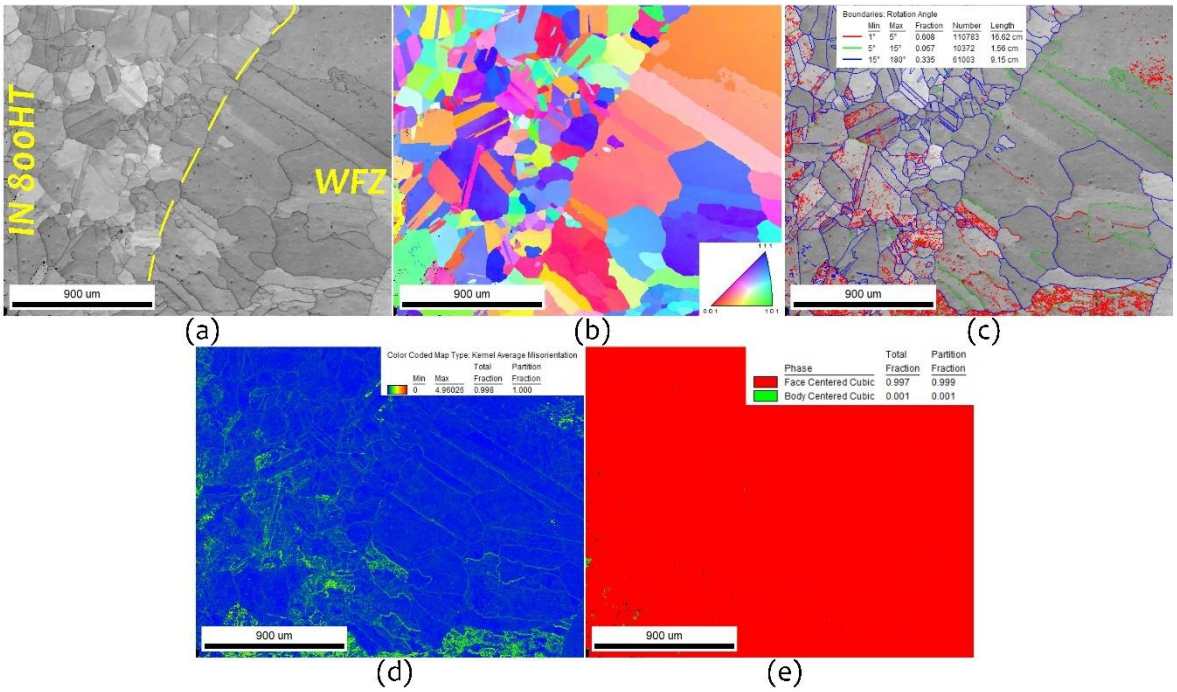


Figure 7.23 : Incoloy 800HT weld interface (a) IQ map (b) IPF map (c) IQ+grain boundary map (d) KAM map (e) phase map

7.4.4 Weld Fusion Zone (WFZ) Microstructure Characterization

The Thermo-Calc-based data was observed to analyze the possibly present phases in A-TIG welded WFZ. In Figure 7.24(a), the possible phases in the matrix were fcc_A1 (gamma prime) in supersaturated solid solution and ordered gamma prime (L12) intermetallic phase. The intermetallic phase is known to precipitate inside the gamma matrix, providing strength to the WFZ. The volume fraction of the gamma phases increases in the matrix at higher temperatures. Both phases may contribute to higher yield strength, but the fcc_A1 phase is also known to cause interphase brittle failure at high temperatures, as predicted. At high temperatures, the formation of the σ-phase was predicted for Incoloy 800HT, which forms majorly in the dendritic regions of the WFZ (Hsieh and Wu, 2012). The WFZ solidification behavior was analyzed with the help of Scheil-Gulliver simulation equations, assuming complete diffusion in the liquid phase having a uniform composition (Lippold et al., 2011). Also, from Figure 7.24(b), thermodynamic simulation in Thermo-Calc shows equilibrium and non-equilibrium behavior of the WFZ solidification at around 1510℃. The equilibrium solidification begins with the formation of ferrite ($L \rightarrow L + \delta$) in the liquid phase at 1510℃. Which completes at 1460℃, then the solidification temperature range (STR) for this reaction to complete was disparaged at 50 ℃ (Hu et al., 2017). The STR, as per Scheil-Gulliver simulation, was 280℃. It predicted the reaction $L + \delta \rightarrow L + \gamma$. Further, solidification proceeds with segregation and continues until the austenite (γ) phase is introduced and until twofold saturation between both phases δ and γ is reached. The solidification ends with invariant reaction $L + \gamma \rightarrow (L + \gamma + M_7C_3)$ at around 1230℃. The solidification process was terminated when the fraction of the solid reached 1.

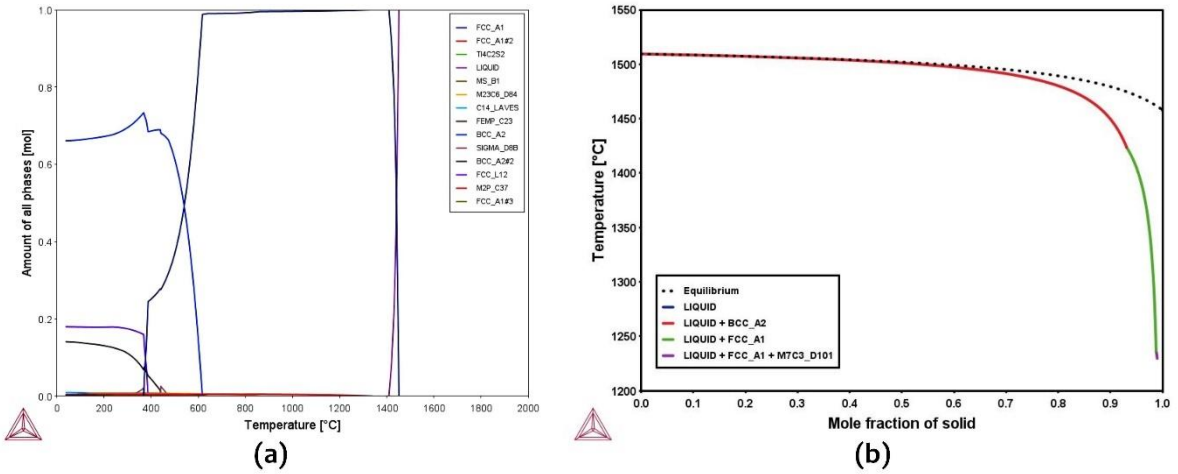


Figure 7.24 : (a) Equilibrium phase diagram for WFZ (b) Equilibrium calculations and Scheil-Gulliver simulation indicating WFZ solidification microstructure evolution

In Figure 7.25(a) the WFZ was found with the dominant presence of cellular dendritic growths with the presence of few columnar dendrites near the weld interface. It was noted that the dendrites were grouped or arranged in packets. The SGBs are the high-angle boundaries of the packets. SSGBs were identified as region/liquid, solidifying the last between the two dendrites. The SGB shown in Figure 7.25(b) micrograph has precipitates deposited over it. Also, small cuboidal precipitates were observed in the WFZ. EDS analysis of the WFZ suggests heavy dilution of Incoloy 800HT in the WFZ. Hence, the austenitic mode of solidification of WFZ occurred. The EBSD scan IQ map in Figure 7.26(a) is the quality micrograph of the WFZ with clearly visible SGBs surrounding the dendrite packets. The IPF map of the WFZ in Figure 7.26(b) shows the grain is preferably orientated in <111> direction, and few are also oriented in <101> direction. Figure 7.26(c) shows the major presence of HAGBs in the WFZ. The SGBs in the WFZ contribute to HAGBs, while a few SSGBs were categorized as MAGBs and LAGBs. The KAM map in Figure 7.26(d) shows a non-uniform distribution of dislocation debris in a few grain or dendritic regions. The SGBs

have some local lattice distortions. The phase map in Figure 7.26(e) demonstrates the predominant prevalence of the fcc phase, with just a nominal proportion of precipitates exhibiting the bcc phase. The generated inverse pole density function (IPDF) plot of WFZ in Figure 7.27(a) shows a clear preferred orientation of grains in WFZ in <111> direction. The orientation distribution function (ODF) sections (φ=0˚, 45˚, 65˚) in Figure 7.27(b) help in analyzing the development of crystallographic texture in the solidified WFZ. The WFZ has shown an austenitic mode of solidification, so the texture of the WFZ was characterized thorough {001}<100> cubic texture, {001}<100> Goss texture, {112}<111> copper texture, and {111}<211> R texture components. Overall, a weaker texture was observed in the WFZ. In Figure 7.28(a), the TEM micrograph shows the SGB in WFZ decorated with Ti-rich precipitates. Figure 7.28(b) shows a cuboidal precipitate in the WFZ, possibly TiC. The cuboidal particle is surrounded by heavy dislocations. While comparing different sections of ODF, the copper texture component hints at high ductility in the WFZ, and the brass component was associated with high mechanical strength. High temperatures and quick cooling can affect the microstructure and crystallographic texture of base metals during welding. The welding process can create new grains and rearrange existing grains, creating a complicated and often uneven microstructure. Goss texture may be seen in the WFZ under certain conditions. However, the base metals' composition, and welding process conditions substantially influence its development.

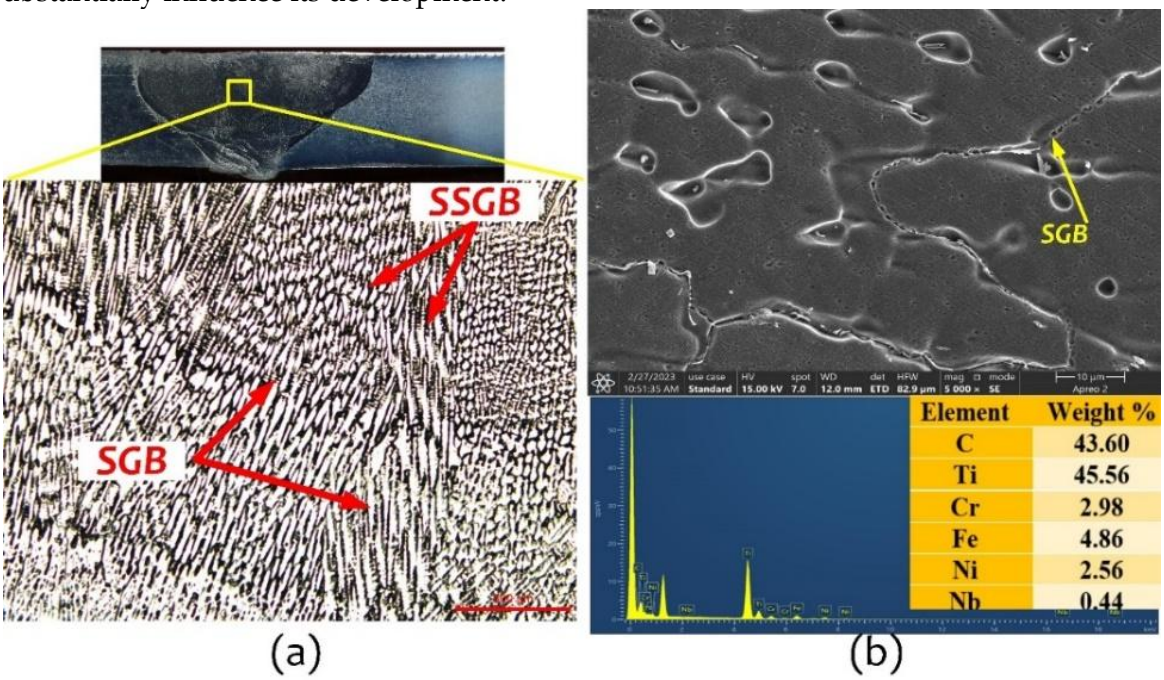


Figure 7.25 : WFZ (a) Optical micrograph (b) FE-SEM micrograph with EDS

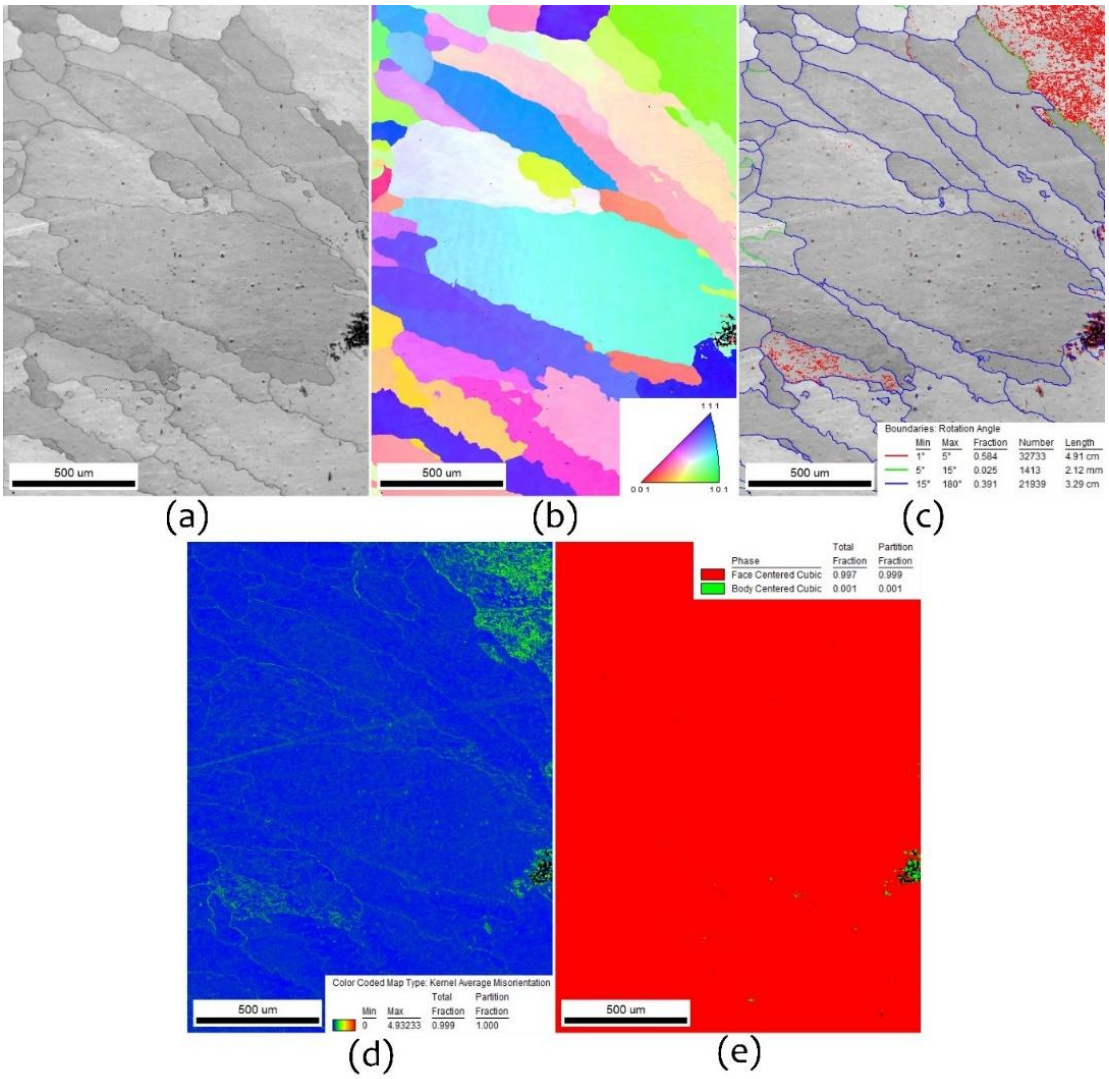


Figure 7.26 : WFZ (a) IQ map (b) IPF map (c) IQ+grain boundary map (d) KAM map (e) phase map

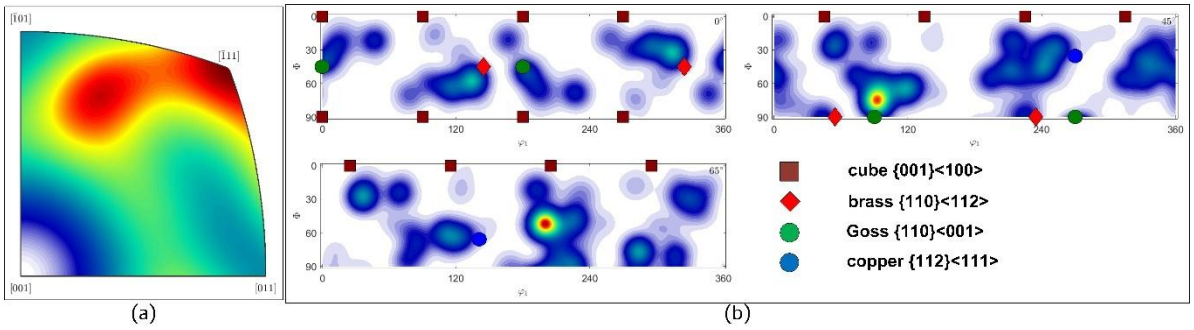


Figure 7.27 : WFZ (a) IPDF plot (b) ODF sections (φ=0˚,45˚, 65˚)

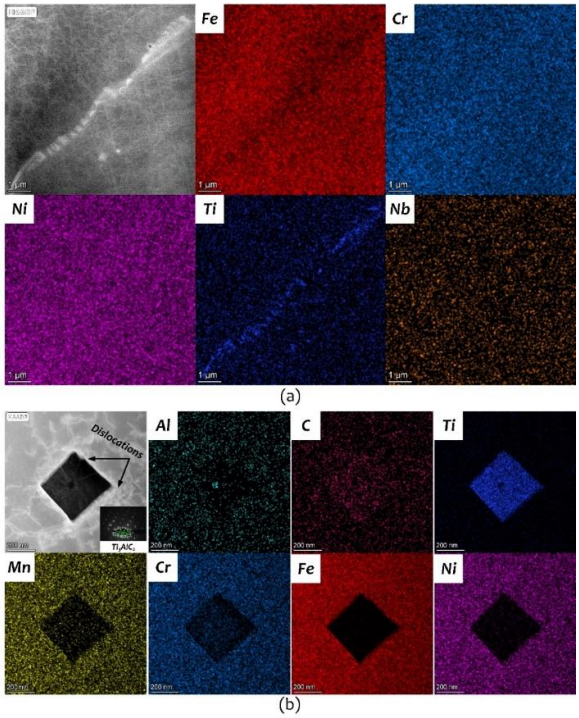


Figure 7.28 : WFZ (a) SGB observed in TEM micrograph with elemental mapping (b) cuboidal precipitate micrograph with SAD pattern and mapping

7.4.5 Tensile Properties

The tensile tests were carried out on specimens prepared as per the ASTM A370 standards (ASTM E8, 2010) for room temperature and high-temperature specimens, and a subsize specimen was extracted to observe the failure in the WFZ. Figure 7.29(a-b) presents the specimens in after testing state, and different failure locations were clearly identified from the visual observation. Table 7.4 summarizes the tensile properties of the tests conducted. The flat as-welded (AW) standard specimen failed from the weakest link of the DWJ, i.e., the Incoloy 800HT base metal side. The observed UTS for the AW standard specimen was 585 ± 5 MPa with YS of 197 ± 5 MPa. The subsize AW specimen failed from the WFZ, giving a remarkable UTS of 706 ± 5 MPa. The specimens were observed with 38% and 36% elongation, respectively. The high-temperature tests were carried out to analyze the DWJ behavior at elevated temperatures. The tests at 650℃ showed failure from the P91 base metal side, and the apparent reason was the limited operating temperature of the P91. The specimen at 650℃ gave a UTS of 178 ± 5 MPa and YS and 44 ± 10 MPa. While at 550℃, the round high-temperature specimen failed from the Incoloy 800HT side, giving a UTS of 306 ± 5 MPa and YS of 56 ± 10 MPa. Both high-temperature specimens showed the flow stress anomaly. Microalloying elements, such as Cr, prefer to segregate along dissociated dislocations at elevated temperatures to lower the stacking fault energy in this occurrence. The matrix's low stacking fault energy facilitates the initiation of deformation twins at high temperatures. Type B+C serrations were observed at a temperature of 550℃ (Figure 7.29(c)). Type B serrations correspond to the phenomenon in which the movement of dislocations is hindered, resulting in a decrease in flow stress as unpinning occurs. Type C serrations occur because of dislocation unlocking at elevated temperatures (Liu et al., 2022). At a temperature of 650℃ (Figure 7.29(d)), the specimen exhibited Type A+B serrations. These serrations were caused by periodic deformations along the specimen's gauge length, resulting in locking Type A serrations (Wright et al., 2012). The engineering stress-strain curves for the tested specimens are plotted in Figure 7.29(e). In the fractography investigation, Figure 7.30(a) shows the fracture surface of the flat AW standard specimen with the presence of dimples and voids. The specimen shows complete ductile behavior that is also reflected from the fractured surface. The flat AW subsize specimen (Figure 7.29(b)) shows mixed-type fracture,

ductile being a major mode of fracture (Mittal and Sidhu, 2015). It also was observed with cleavage facets. The brittle nature could be due to the stress concentration around any secondary phases formed in the WFZ, which may have provided the nucleation site to form a micro crack. For round high-temperature specimens, 550°C (Figure 7.30(c)), the failure surface of Incoloy 800HT shows a mixed mode of failure and ductile being dominant. The Incoloy 800HT matrix at high temperature was observed with the evolution of fine-sized precipitates and, due to the coarsening of secondary phases present in the matrix, promoted the crack propagation along the weak planes in the crystal lattice. At 650°C (Figure 7.30(d)), the perfect cup-cone type failure surface was observed, representing the ductile mode of failure from the P91 side. The P91 at this temperature is reported to experience carbide precipitation at grain boundaries and matrix, this led to grain coarsening and grain boundary migration. Further, grain boundaries act as nucleating sites for void formation as grain size increases due to coarsening. Similar results were reported using A-TIG welding technique, where the UTS of the WFZ increased significantly (Pavan et al., 2023; Sharma and Dwivedi, 2019).

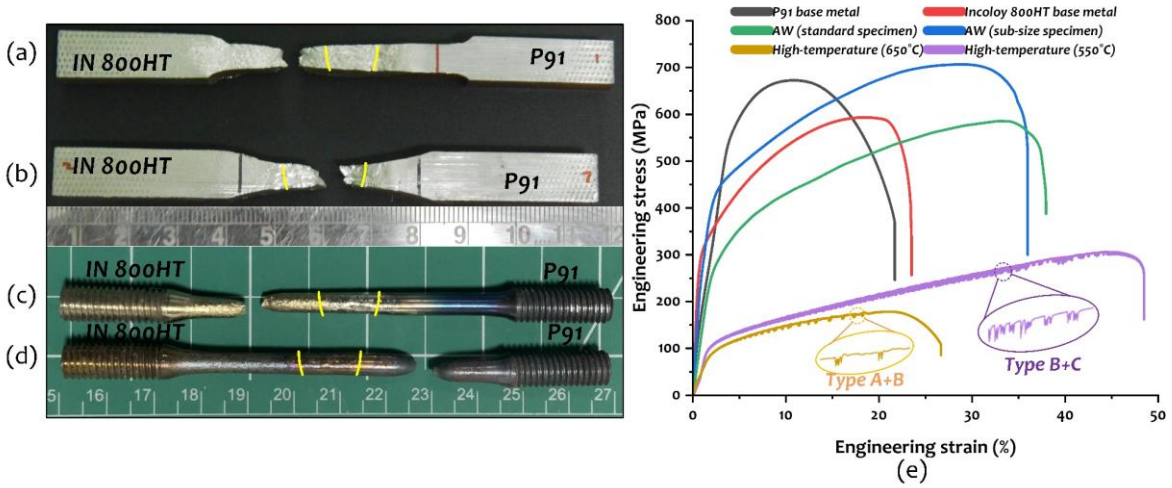


Figure 7.29 : Tensile specimen after testing (a) AW standard flat room temperature specimen (b) AW subsize flat room temperature specimen (c) high-temperature (550°C) round tensile specimen (d) high-temperature (650°C) round tensile specimen (e) engineering stress-strain curves for tested tensile specimens

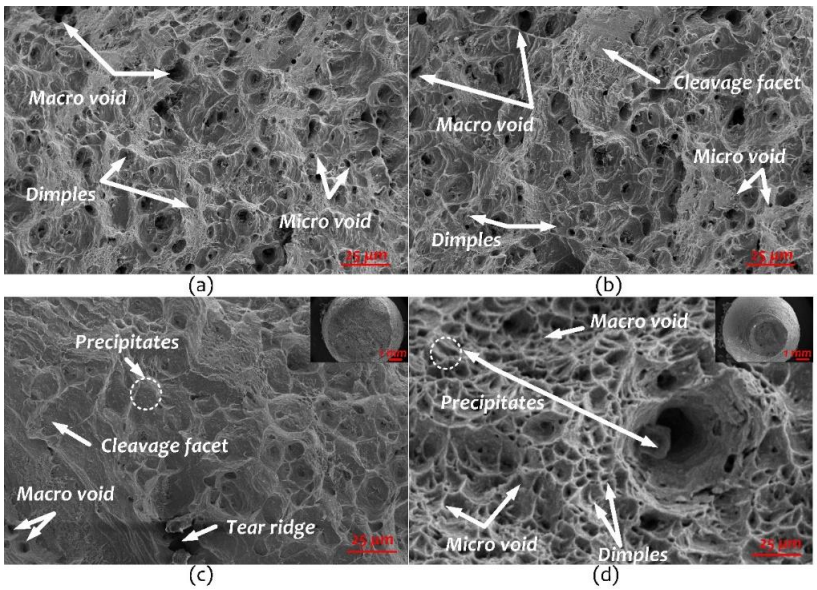


Figure 7.30 : FE-SEM micrographs (a) AW standard flat room temperature specimen (b) AW subsize flat room temperature specimen (c) high-temperature (550°C) round tensile specimen (d) high-temperature (650°C) round tensile specimen

Table 7.4 : Tensile strength observed for different specimens

Specimens	*UTS (MPa)*	*YS [offset 0.2%] (MPa)*	*Elongation (%)*	*Reduction in the area (%)*	*Failure site*
AW (Standard specimen)	585 ± 5	202 ± 5	38 ± 2	24 ± 2	Incoloy 800HT base metal
AW (Subsize specimen)	706 ± 5	-	36 ± 2	21 ± 3	WFZ
High-temperature (650°C)	178 ± 5	44 ± 10	27 ± 2	38 ± 3	P91 base metal
High-temperature (550°C)	306 ± 5	56 ± 10	48 ± 3	54 ± 3	Incoloy 800HT base metal

7.4.6 Microhardness Properties

The Vickers microhardness measurements were performed across the WFZ of the DWJ. The indents were taken at a 0.5mm gap, as shown through the schematic in Figure 7.31. Also, a significant variation in the microhardness was witnessed in the P91 HAZ region of the DWJ. The peak microhardness of 345 ± 5HV was found in the CGHAZ region and a minimum of 210 ± 5HV in the ICHAZ region. The FGHAZ region in P91 HAZ had an average microhardness of 265 ± 10HV. The WFZ was observed with an average microhardness of 227 ± 10HV. The maximum value of 260 ± 5HV was observed near the center of the WFZ. The Incoloy 800HT HAZ was observed with a stable microstructure, so the average microhardness variation in the region was 181 ± 10HV, similar to the average microhardness of 178 ± 10HV observed in the Incoloy 800HT base metal side. The CGHAZ in the P91 HAZ experienced high levels of microhardness due to the formation of untempered martensite. ICHAZ drop was witnessed due to the presence of over-tempered martensite in the region. Hence, PWHT is recommended to homogenize the variation observed in P91 HAZ (Arivazhagan et al., 2009; Sudha et al., 2006). The WFZ also witness an odd increase in microhardness in the WFZ center, probably due to the formation of secondary phases in the dendritic cores (Bhoskar et al., 2023; Kalyankar et al., 2022). For A-TIG welding technique, if compared with conventional welding techniques, the HAZ region witnessed less severe variation in the microhardness, and the peak microhardness recorded for the CGHAZ region was also comparatively less (Arivazhagan and Vasudevan, 2014; Divya et al., 2014; Pandey, 2020; Shanmugarajan et al., 2011).

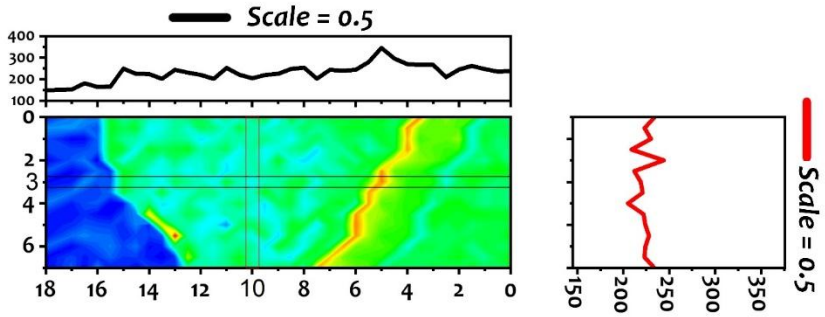


Figure 7.31 : Contour microhardness variation plot for the P91 and Incoloy 800HT DWJ

7.4.7 Charpy Impact Toughness

The AW specimens were subjected to Charpy impact toughness testing with a V-notch machined along the WFZ. The specimen prepared per the ASTM A370 standard is displayed in Figure 7.32(a). Also, the fractured specimen after the impact is shown in Figure 7.32(a). It was determined that the AW specimen had a ductile mechanism of failure since it

had shear lips and a lateral expansion. The fracture traveled completely along the WFZ. The specimen had a Charpy impact toughness rating of 96 ± 5 J. This suggests that the DWJ between P91 and Incoloy 800HT had a significant Charpy impact toughness to surpass the benchmarked toughness standards. The WFZ fractured surface was observed with a mixed mode of failure in the fractography (Figure 7.32(b)) (Anand et al., 2016). The results are in coherence with the observations reported for a similar A-TIG DWJ with Incoloy 800 interlayer (Kulkarni et al., 2020), where the high Charpy impact toughness and dominant ductile behavior were attributed to the formation of austenitic structure and multiple slip systems in the fcc phase observed in the WFZ.

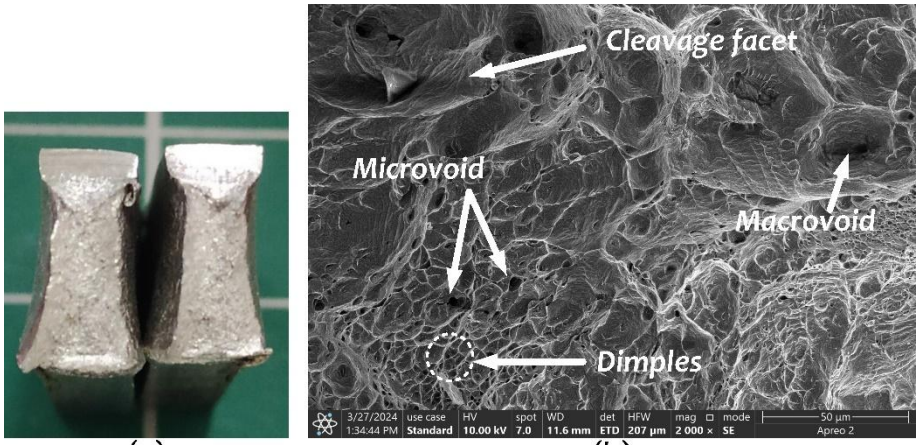


Figure 7.32 : (a) Fractured specimen (b) FESEM micrographs of V-notch Charpy impact toughness specimen